Relativistic attosecond electron pulses by laser wakefield acceleration

Cornelia Gustafsson

LUND
UNIVERSITY

Division of Atomic Physics, LTH
Lund, Sweden
October 2020

PHYM01
Degree Project (30 credits ECTS)
LRAP 568
Supervisor: Olle Lundh
Examiner: Jörgen Larsson

Abstract

The search for cheaper and more compact accelerators has led to the development of laser-driven plasma-based accelerators. In comparison to conventional particle accelerators, the plasma-based accelerator is inherently insensitive to the breakdown of the acceleration structure and therefore greater accelerating fields can be obtained. One such setup, which is used to accelerate electrons, is the laser wakefield accelerator. Behind the laser, an electric field gradient of the order of hundreds GV/m can be obtained as the intense laser pulse propagates through the plasma, and electrons submitted to this field can be accelerated to several MeV over just few millimeters. During 2020, the Division of Atomic Physics at Lund University will purchase a new laser system, and in comparison to the old system, the new laser system has a shorter pulse duration, lower energy, and higher repetition rate. Through particle in cell simulations, it has in this thesis been shown that attosecond electron pulses can be achieved with the parameters of the new laser system. The duration of the electron pulses is tuned by modulating the plasma density. The energy of the these short electron pulses are of the order of tens of MeV. However, for the specified plasma density, it is more beneficial to drive the wakefield by a laser with four times the energy than the system the upgraded laser system the Division plans to purchase. The energy spectrum of the accelerated electrons at this laser energy proved to be more peaked, and the electrons could be accelerated over a longer distance than if the energy of the upgraded laser system were utilized.

Populärvetenskaplig sammanfattning

Generering av ultrakorta elektronpulser med hjälp av laseracceleration

Hur snabb är den snabbaste processen som vi kan observera? Och hur litet är det minsta objektet? Kort sagt så kan vi inte se snabbare än vad ett slutarljus tillåter, eller objekt mindre än den minsta möjliga våglängden.

Vad menar jag då med det? Jo, om vi vill ta stillbilder av en galopperande häst, utan att bilden blir suddig, måste vi ha en blixt eller slutarljus som är snabbare än hästen. Vill vi nu kunna se biologiska eller kemiska reaktioner som sker så snabbt som knappt några miljondels miljarddels sekunder, måste alltså slutarljuset vara lika snabbt eller snabbare! Dessutom kan molekylerna, och framförallt de individuella atomerna, vara mycket små, och med samma tankegång som med slutarljuset, måste våglängden hos ljuset vara i motsvarande längd som det vi vill se. Så, en atom som är omkring 1000 gånger mindre än ett hårstrå, kräver en lika "lång" våglängd. Vi är i röntgenområdet, och härifrån växer utmaningarna.

Ett sätt att generera kort röntgenstrålning är med hjälp av en plasmavåg, och i jämförelse med en konventionell accelerator, används en laser för att excitera plasmavågen som elektronerna kan surfa på. När en laser av mycket hög intensitet fokuseras i en gas är kraften från lasern så stor att gasen fullständigt joniseras. Elektronerna slås ut och bort från fokuspunkten, och precis bakom lasern bildas ett område helt tomt på elektroner. Gasen joniseras fullständigt och lasern bildar alltså ett plasma. Trycket från lasern gör så att elektronerna slungas uppåt och bakåt. Samtidig strävar de efter att återförenas med de positiva jonerna, men på grund av den höga kraften hos lasern kommer de i stället att svänga runt sin jämviktspunkt utan bindas till dem. Det har bakom lasern bildats en bubbla, likt kölvattnet bakom en motorbåt. En bild som illustrerar hur bubblan ses i Fig. 1.

Om nu bubblan betraktas mer ingående, så ses det att; precis bakom lasern är nettoladdningen positiv, och på baksidan av den bildade bubblan är nettoladdningen negativ. Alltså har det över hela bubblan bildats ett starkt elektriskt fält där elektroner kan accelereras. För att elektronerna ska kunna se fältet, måste de *injiceras* i bubblan. När injectionsprocessen upphör, klumpar elektronerna ihop sig och bildar en puls som nu kan accelereras i fältet. Dessa elektroner når en hastighet nära ljusets hastighet i vakuum. Samtidigt som elektronerna drivs i framåtriktningen med

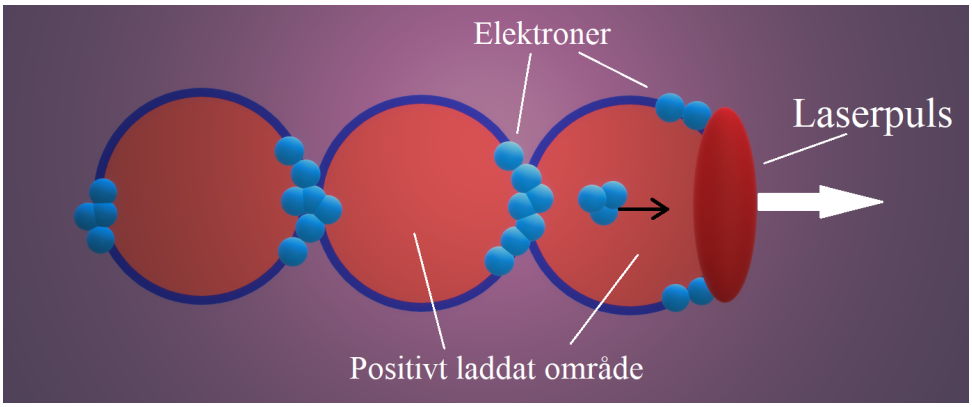

Fig. 1: *Bild som illustrerar växelverkan mellan en mycket stark laserpuls och en gas. Laserns intensitet är såpass hög att elektronerna fullständigt slås bort och lämnar ett område bakom lasern helt fritt från elektroner. I bubblan kan elektroner accelereras i en riktning som illustreras av den svarta pilen i figuren.*

lasern, svänger de också transversellt, vilket ger upphov till röntgenstrålning. Detta är vad som ligger till grund för så kallad *Laser wakefield acceleration* (LWFA), som direktöversatt till svenska blir "Laser- kölvattensfältacceleration". Vad är då fördelen med att använda sig av den här typen av acceleratorer? För det första kan väldigt höga elektriska fält uppnås bakom lasern. Det medför att på bara några centimeter kan mycket höga partikelenergier uppnås, medan motsvarande energier in en konventionell accelerator kräver mycket längre sträckor. Dessutom blir acceleratorn liten och kostnadseffektiv, vilket öppnar upp möjligheten för lokala röntgenkällor i laboratorier och sjukhus. Det här blir viktigt när syftet är att generera röntgenstrålning med till exempel hjälp av en frielektronlaser (FEL), som förlitar sig på att elektronerna rör sig en viss sträcka en enstaka gång. För det andra så kan då pulslängden av elektronerna göras mycket kort, upp mot en bråkdel av en miljondels miljarddels sekund, vilket genererar motsvarande kort röntgenpuls.

Atomfysikavdelningen vid LTH kommer under 2020 att upphandla ett nytt lasersystem, och i jämförelse med det tidigare systemet så har den nya lasern kortare pulslängd, lägre pulsenergi, och skickar fler antal ljuspulser per sekund. Det är då intressant att undersöka om det är möjligt att generera elektronpulser som är en miljon miljard gånger kortare än en millisekund i ett LWFA experiment och som följd motsvarande röntgenstrålning. Med så kort röntgenstrålning är det möjligt att undersöka biologiska, kemiska, och fysiska processer. Jag har genom simuleringar, där jag använt mig av en skräddarsydd densitetsprofil av plasmat, visat på att mycket korta elektronpulser kan generaras med det nya lasersystemet. Pulserna har en längd av en bråkdel av en miljon miljarddels sekund, och generering av korta pulser kan förväntas experimentellt också.

Acknowledgements

I would like to start by thanking my supervisor, Olle Lundh, for the support and guidance, and raising an interest in this subject already when I just arrived in Lund two years ago. Jonas Björklund Svensson, for the invaluable feedback and at the early stage of this report, the support, and the amount knowledge I was able to take part of. Henrik Ekerfelt for helping me out with analyzing and understanding the simulations. Diego Guenot for the support and brief introduction to few cycle pulses. Alexander for saving me from the computer before I was quarantined, and Giada for being a great office pal (those few times I have been there) and for the support. Also, those in the high intensity group not mentioned here, thank you for including me in your group. I have learned a lot from all of you, more than I expected. Lastly, but absolutely not least; my greatest critic and supporter through all times, Marc Nilsson.

Thank you!

Contents

1

Introduction

An accelerator based radiation source has a number of applications, such as in materials sciences, industry, medicine and more. In materials sciences, it could for example be interesting to resolve individual molecules, and the corresponding wavelength must be as short or shorter than the smallest molecule resolved. If even smaller structures are to be resolved, such as atoms, with a radius of the order of 10^{-10} m, then again, the wavelength must be of the same order of magnitude or smaller. Therefore, the wavelength range needed to resolve atoms are in X-ray regime. These can for example be obtained from accelerating electrons. In "conventional" accelerators, particles are driven by radio frequency (RF) electromagnetic waves, while magnets focus the particles and bend their trajectories. By accelerating the particles over a longer distance, higher energies can be obtained, but as the energy increases, so must the strength of the magnets. Still, the conventional accelerators are limited to accelerating fields of a few MV/m before the breakdown of the cavity walls occur. Therefore, the accelerators must be made several meters long in order to produce high energetic particles. For example, the linear accelerator (Linac) at MAX IV Lund, has an approximate length of 300 m and a nominal particle energy of 3.0 GeV [1]. The electron pulses from the accelerator are readily prepared to be sent to the short pulse facility (SPF), to produce sub-ps X-rays at MAX IV. However, ultra-short X-ray pulses, down to a duration of a few fs, and even sub-fs, with high-quality are demanded in research [2]. A conventional accelerator delivering these ultra-short and high energetic X-rays would be large, several hundreds of meters and even kilometers long, and consequently the construction cost expensive [3].

In 1979, Tajima and Dawson [4] proposed a laser driven plasma-based accelerator, for which an accelerating field exceeding several GV/m could be obtained. These accelerators requires laser pulse intensities of the order of 10^{18} W/cm^2, and at the Division of Atomic Physics at Lund University, LWFA experiments are made possible with the TW-laser system. The electron pulses from the accelerator can then either be used as a X-ray source, where the radiation from the transverse oscillation of the accelerating electrons in the bubble regime is directly used, or the electrons after leaving the regime can be used as a driver for example an FEL. In comparison to a conventional RF-accelerator, the plasma can withstand the high accelerating

field, and if driven by short laser pulses, in the order of a few fs, the resulting electron pulse will be inherently short as well. This ultimately also means that over a distance significantly shorter than that of current existing accelerators, potentially hundreds of micrometers, the accelerated electrons will have gained more energy than otherwise obtainable. The short structure opens up the possibility of tabletop, cost-effective accelerators [3].

When a laser pulse of very high intensity interacts with gas, it may be completely ionized, creating a plasma. The electrons are expelled away from the laser's focus, and just behind it, a bubble completely evacuated of electrons is created. Across the bubble, the electric field is such that right behind the laser, it is positive, and at the back it is negative. The whole structure can then be thought of as a capacitor. In this bubble, electrons can be injected, forming an electron pulse, and then accelerated. This is the foundation of *Laser Wakefield Acceleration* (LWFA). As will be shown in this report, the bubble depend on the spot size of the laser, and the size of the bubble will determine the spatial length of the electron pulse. Since interaction between the intense laser and plasma will be highly nonlinear, the plasma will act as a focusing lens as the laser propagates through it. Furthermore, the focusing effect is dependent on the plasma density. Therefore, in an LWFA, the spatial pulse length of the electron pulses can be further compressed by modulating the spatial geometry of the plasma [2, 5, 6, 7]. However, the accelerating structure of an LWFA is small, typically a few μm, and the accelerating effects are transient. This, together with the complexity of the mechanism that makes the electrons subjected to the accelerating field makes the diagnostics challenging. Therefore, simulations are often used together with experimental results, and a common powerful tool is the *particle in cell* (PIC) method. With the simulation, various effects can be isolated an investigated individually [8].

Today, there are several different PIC algorithms, but they all have in common that the field is represented on a grid, while the physical particles, i.e., electrons and ions, are grouped together to so called macroparticles. The algorithm then couples the kinetics of the macroparticles to the fields represented on the grid [9]. What then essentially differs between the different existing PIC-codes are how the decomposition of the field is done mathematically. In this project, the *Fourier-Bessel particle in cell* (FBPIC) algorithm is used [10], which is a PIC-code performing calculations with a cylindrical geometry, and the field is decomposed by Fourier-decomposition. It is motivated in this report that the FBPIC algorithm is computationally fast and accurate for geometries close to cylindrical, such as an LWFA. In particular, the code is used to simulate the new laser parameters, to investigate the production of ultra-short electron pulses.

1.1 Background

During 2020, the Division of Atomic Physics at the physics department of Lund University, will purchase a new laser system that will be used in research involving high intensity lasers, including LWFA experiments. In comparison to the current

laser system, the new laser will have a lower pulse energy, shorter pulse duration, and higher repetition rate. A compilation of the two laser systems can be seen in table 1.1. For this degree project, it is of particular interest to investigate if it is possible to generate attosecond electron pulses with the new laser parameters.

Table 1.1: *Specifications of the current and new laser system.*

Parameter	**Current laser system**	**New laser system**
Pulse energy [mJ]	1000	50
Pulse duration [fs]	30	7
Repetition rate [Hz]	5	100
Center wavelength [nm]	800	800

What is interesting about generating attosecond electron pulses is that the corresponding X-ray radiation will have a similar duration, which then makes it possible to examine ultrafast phenomena, such as charge migration in electronics and biological processes [11]. By performing simulations, using the FBPIC algorithm, LWFA is studied with the new laser parameters.

1.2 Purpose and question at issue

The purpose of this degree project, is to simulate the LWFA by using the FBPIC algorithm with the parameters of the new laser system as defined in table 1.1. The following issues are investigated:

- Can ultra-short ($<$ 1fs) electron pulses be generated?
- What is the particle energy?
- What is the energy spread?

The study is done by performing the simulations for different density modulations of the plasma. As will be motivated in section 3.5, the change in electron density of the plasma directly affects plasma wave, and consequently the electron pulse duration.

1.3 This thesis

The project is limited to the highly relativistic and nonlinear interaction between short laser pulse and a gas, where the laser intensity is such that the gas completely ionizes the gas. The laser has thus created an underdense plasma (a more precise definition can be found in section 2.2). Chapter 2 gives a brief description of electromagnetic fields and plasmas in order to understand the underlying physics of an LWFA. In chapter 3, the physics of LWFA is described. The theory is explained starting from a 3D linear interaction and then adapted to the nonlinear regime. In chapter 4, the principles of PIC algorithms is explained, and then the FBPIC. Chapter 5 presents the simulation results of this project together with a discussion. The report is concluded with chapter 6 with conclusions and outlook.

2

Electromagnetic waves and plasmas

This chapter introduces the concept of electromagnetic waves and plasmas needed to understand the underlying physics of an LWFA.

2.1 Electromagnetic fields in vacuum

The theory in this section closely follows chapters 2, 3, and 5 from [12]. One of the reasons why light can travel through vacuum is because it consists of two orthogonal fields, the electric and magnetic field. These two fields are related to each other by Maxwell's equations:

$$\begin{aligned} \nabla \times \mathbf{B} &= \mu_0 \left(\mathbf{j} + \varepsilon_0 \frac{\partial \mathbf{E}}{\partial t} \right), \\ \nabla \times \mathbf{E} &= -\frac{\partial \mathbf{B}}{\partial t}, \\ \nabla \cdot \mathbf{E} &= \frac{\rho}{\varepsilon_0}, \\ \nabla \cdot \mathbf{B} &= 0, \end{aligned} \tag{2.1}$$

where $\mathbf{E}$, is the electric field, $\mathbf{B}$ the magnetic field, ρ the total electric charge density, and $\mathbf{j}$ the current density. The constants, μ_0 and ε_0 are the vacuum electric permittivity and magnetic permeability and the product of these two constants define *the speed of light in vacuum*, $c = \sqrt{1/(\varepsilon_0 \mu_0)}$.

All light, laser pulses included, propagates as waves, and in vacuum they travel with a constant speed, c. The wave may mathematically be described by the complex wave equation:

$$\psi(\mathbf{r}, t) = \mathfrak{a}(\mathbf{r}) \exp\{i(\phi(\mathbf{r}) + \omega t)\}, \tag{2.2}$$

where $\mathbf{r} = (x, y, z)$ is the spatial position, t is the time, $\phi(\mathbf{r})$ the phase, $\mathfrak{a}(\mathbf{r})$ the amplitude, and ω the angular frequency. To represent an optical wave, the wave equation must satisfy the wave function, such that:

$$\nabla^2\psi - \frac{1}{c^2}\frac{\partial^2\psi}{\partial t^2} = 0, \tag{2.3}$$

where $\nabla^2 = \partial^2/\partial x^2 + \partial^2/\partial y^2 + \partial^2/\partial z^2$ is the Laplacian operator. The wave equation in Eq. (2.2) can be represented on the form $\psi(\mathbf{r}, t) = \psi(\mathbf{r})\exp(i\omega t)$, where $\psi(\mathbf{r}) = \mathfrak{a}(\mathbf{r})\exp(i\phi(\mathbf{r}))$ is the complex amplitude. Substituting this representation into Eq. (2.3) will now lead to the time independent *Helmholtz equation*:

$$\nabla^2\psi + k^2\psi = 0, \tag{2.4}$$

where $k = \omega/c$, is called the wavenumber. Depending on the chosen boundary conditions, different solutions arise. One of the simplest solutions is the plane wave:

$$\psi(\mathbf{r}, t) = |\mathfrak{a}(\mathbf{r})|\cos(\omega t - kz + \phi(\mathbf{r})). \tag{2.5}$$

The equation thus says that the wave propagates in the positive z-direction, with a certain angular frequency, ω, and with a certain phase $\phi(\mathbf{r})$. In terms of an electromagnetic wave, with center frequency ω_0, the plane wave can be expressed as:

$$\mathbf{E}(z) = E_0\cos(kz - \omega_0 t)\mathbf{e}_x. \tag{2.6}$$

The amplitude of the plane wave may in vacuum be related to the amplitude of the magnetic field through the expression $|\mathbf{B}| = |\mathbf{E}|/c$. For the electromagnetic plane wave, the intensity, i.e., the power per unit area, can be expressed in terms of the electric field amplitude as:

$$I_0 = c\varepsilon_0\frac{|E_0|^2}{2}. \tag{2.7}$$

To describe the interaction between a laser beam and a plasma, it is often convenient to use the vector potentials of the electric and magnetic field, which in vacuum becomes [3]:

$$\begin{aligned}\mathbf{E} &= -\frac{\partial \boldsymbol{A}}{\partial t},\\ \mathbf{B} &= \nabla\times\boldsymbol{A}.\end{aligned} \tag{2.8}$$

Therefore, the plane wave in Eq. (2.6) may be expressed terms of the vector potential as:

$$\mathbf{A}(z) = A_0\sin(kz - \omega_0 t)\mathbf{e}_x, \tag{2.9}$$

where $A_0 = E_0/\omega_0$ is the amplitude of the vector potential. In this report, unit vectors will be denoted $\mathbf{e}_i$, where i denotes the Cartesian coordinate. Hence, $\mathbf{e}_x$ is

the unit vector along x, and describes the polarization direction.

Another solution to Eq. (2.4), and a rather important one, is obtained if it assumed that the beam mainly travels in the z-direction, such that it makes a small angle with the propagation axis. The solution is the Gaussian beam, which is an idealization of a laser beam, also a laser pulse. The complex amplitude of a laser pulse is therefore described by:

$$\begin{aligned}\psi(\mathbf{r},t) =& \mathfrak{a}_0 \frac{w_0}{w(z)} \exp\left(-\frac{x^2+y^2}{w^2(z)}\right) \exp\left(-ikz - ik\frac{x^2+y^2}{2R(z)} + i\zeta(z)\right) \times \\ & \exp\left(-2\ln(2)\frac{t^2}{\tau_0^2}\right) \exp(i\omega_0 t),\end{aligned} \tag{2.10}$$

where $\mathfrak{a}_0$ is a constant, $w(z)$ is the beam radius at any position z, and $\zeta(z)$ is called the Gouy phase, and describes the additional phase pick-up of a Gaussian wave in comparison to a plane wave and a spherical wave, which is another solution to Eq. (2.4), not treated in this report. $R(z)$ is the radius of curvature, which describes the curvature of the wavefront at any position z, and lastly, $w_0 = \sqrt{\lambda Z_R/\pi}$ is called the beam waist, where $\lambda = 2\pi c/\omega$ is the wavelength and Z_R the Rayleigh length. The Rayleigh length defines the distance on the optical axis over which the intensity of a laser has dropped to $1/2$ of its maximum value. Moreover, it defines the depth of focus, i.e., the distance over which the laser remains "sharp", which for a Gaussian beam is $2Z_R$. The time dependent part of the equation describes the envelope of the laser pulse, where τ_0 is the temporal width at the full width of the half maximum (FWHM) of the pulse.

The beam waist, w_0, is where the Gaussian beam's width is the smallest, or, where the maximum intensity of the beam has dropped by a factor of $1/e^2 \approx 0.135$. In beam optics, which these definitions has been derived from, the maximum intensity, or the peak intensity, is defined by:

$$I_0 = \frac{2W}{\pi w_0^2 \tau_0} \tag{2.11}$$

where W is the laser pulse energy, and the optical power of the laser can be defined as $P = W/\tau_0$.

In terms of an electromagnetic wave that is linearly polarized in the x-direction, the Gaussian beam becomes:

$$\mathbf{E}(\mathbf{r},t) = E_0 \mathbf{e}_x \psi(\mathbf{r},t), \tag{2.12}$$

where $\psi(\mathbf{r})$ is the complex amplitude defined in Eq. (2.10), and E_0 the electric field amplitude.

2.2 Electron propagation in the laser field

The motion of a single electron subjected to an electromagnetic field, such as the laser field, is described by the Lorentz equation [13]:

$$\frac{d\mathbf{p}}{dt} = -e(\mathbf{E} + \mathbf{v} \times \mathbf{B}), \tag{2.13}$$

where $\mathbf{v}$ is the velocity of the electron and $\mathbf{p} = \gamma m_e \mathbf{v}$ the electron momentum, and $\gamma = (1 - \beta^2)^{-1/2}$ the relativistic factor and $\beta = v/c$ is the normalized velocity of the electron, where v is its speed. The $\mathbf{E}$-field is responsible the excitation of a linear plasma wave, and $\mathbf{v} \times \mathbf{B}$, as will be shown, causes the excitation of a nonlinear plasma wave [3]. Since the electric field, $\mathbf{E}$, is transverse to the propagation direction of the laser, the electrons will wiggle in the same direction. This field alone can not accelerate the electrons, at least not in free space.

Since the magnitude of the magnetic field of a plane wave could be expressed as $|\mathbf{B}| = |\mathbf{E}|/c$, as mentioned in section 2.1, for non-relativistic electrons with ($\beta \ll 1$), the second term on the right hand side in Eq. (2.13) can be neglected. With a classical approach, the electrons initially at rest at position $z = 0$ will oscillate with a velocity:

$$\begin{aligned} \ddot{z}(t) &= -\frac{eE_0}{m_e}\cos(\omega_0 t) \Rightarrow \\ \dot{z}(t) &= v = -\frac{eE_0}{m_e\omega_0}\sin(\omega_0 t), \end{aligned} \tag{2.14}$$

which then leads to the normalized velocity:

$$\beta = -\frac{eA_0}{m_e c}\sin(\omega_0 t), \tag{2.15}$$

from which the normalized vector potential now is defined as:

$$a_0 = \frac{eA_0}{m_e c}. \tag{2.16}$$

The normalized vector potential, a_0, is a recurring parameter when chracterizing the interaction between an intense laser pulse and plasma. For a linearly polarized Gaussian pulse, the laser power and a_0 are related by [3]:

$$P \simeq 21.5\left(\frac{a_0 w_0}{\lambda_0}\right)^2 \quad [\text{GW}]. \tag{2.17}$$

When $a_0 \gtrsim 1$, the electron's velocity approaches c, and it becomes relativistic, which means that the term $\mathbf{v} \times \mathbf{B}$ in Eq. (2.13) no longer can be neglected. In the frame which is co-propagating with the laser pulse, the vector potential becomes $\boldsymbol{a}(z,t) = e\boldsymbol{A}/m_e c = a_0 \sin(k_0\xi)$, where $\xi = z - ct$ gives the coordinate in the co-propagating frame [3]. The effect that the magnetic field has on the electrons can

be derived from first finding the expression of the normalized momentum, which in the x and z direction are [14]:

$$\begin{aligned} u_x &= \gamma\beta_x = \frac{dx}{d\xi} = \boldsymbol{a} = a_0 \sin(k_0\xi) \\ u_z &= \gamma\beta_z = \frac{dz}{d\xi} = \frac{\boldsymbol{a}^2}{2} = \frac{a_0^2}{2}\sin^2(k_0\xi). \end{aligned} \tag{2.18}$$

Integrating Eq. (2.18), the displacement in each direction can are obtained as:

$$\begin{aligned} x &= -\frac{a_0}{k_0}\cos(k_0\xi) \\ z &= \frac{a_0^2}{8k_0}\left(2k_0\xi - \sin(2k_0\xi)\right). \end{aligned} \tag{2.19}$$

Investigating Eq. (2.18) and (2.19), it is firstly observed that in the z-direction, the velocity is always positive. Hence, $\mathbf{v} \times \mathbf{B}$ pushes the electrons forward, i.e., it is responsible for the acceleration in the direction of the laser propagation and, as will be shown, the nonlinear ponderomotive force. Secondly, as the electron moves forward in z, it oscillates longitudinally at a frequency twice the laser frequency. Also, when $a_0 \gtrsim 1$, the longitudinal oscillations dominate over the transverse. However, in order to obtain a nonlinear response from the laser and plasma interaction, a non-uniform laser profile must be used, such as a Gaussian pulse. The laser can be tightly focused and high intensities can consequently be obtained. The ponderomotive force, explained in section 3.1, then excites a plasma wave, which transfers the energy from the laser to the electrons [3].

2.3 Electromagnetic fields in a plasma

In an LWFA, a laser pulse of very high intensity is focused onto a gas, and completely ionizes it, creating a plasma. A plasma is a state of matter, consisting of free negative and positive charges, i.e. free electrons and ions. The net charge of a plasma however, is zero. Because of the very high intensity of the laser in an LWFA, the dominating ionization effect in LWFA is called over-the-barrier-ionization. In comparison to photoionization, where a photon with an energy matching the ionization energy of the atom or higher "lifts" the electron from the system, the electric field is now such that the electron potential is heavily disturbed. The electrons are then released into the continuum and subjected to the electric field of the laser alone. A figure showing the principle of over the barrier ionization can be seen in Fig. 2.1 [15]. Since the laser field oscillates, over the barrier ionization can occur every half-cycle of the laser oscillation.

2.3.1 Laser propagation in a plasma

In the presence of an electromagnetic field, the plasma electrons which are much lighter than the ions, will oscillate around their equilibrium position with a charac-

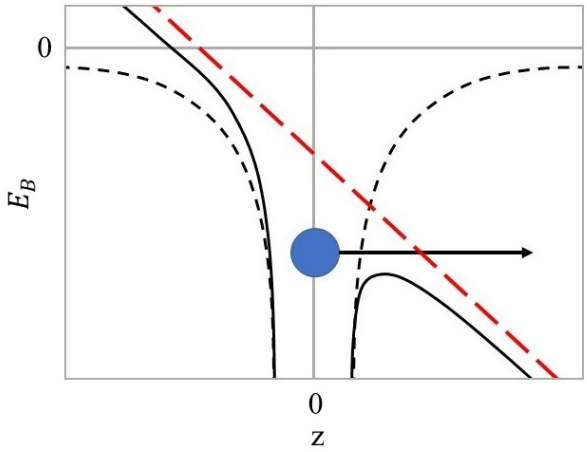

Fig. 2.1: *Over-the-barrier ionization. The dashed black lines are the undisturbed potential barrier, while the heavy black lines shows the potential disturbed by the very intense electric field of the laser, illustrated by the red dashed line. The blue dot is the electron, and E_B its binding energy.*

teristic frequency, called the plasma frequency [14]:

$$\omega_p = \sqrt{\frac{n_e e^2}{m_e \varepsilon_0}}, \tag{2.20}$$

where n_e is the plasma electron number density, e the elementary charge, m_e the electron's rest mass. The plasma frequency describes the longitudinal oscillation in plasma number density. For an electromagnetic wave, with fundamental frequency ω_0, propagating in the plasma, the following dispersion relation can be written as [14]:

$$\omega_0^2 = \omega_p^2 + c^2 k^2, \tag{2.21}$$

where k the wavenumber of the electromagnetic wave. Solving for k yields:

$$k = \frac{\sqrt{\omega_0^2 - \omega_p^2}}{c}. \tag{2.22}$$

Hence, three limits for the laser frequency arises. When $\omega_0 > \omega_p$, k is real, and the laser can propagate through the plasma. For $\omega_0 < \omega_p$, k becomes imaginary, and the electromagnetic wave can not propagate through the plasma. Lastly, when $\omega_0 = \omega_p$, a critical density, n_c, can be defined as:

$$n_c = \frac{\omega_0^2 m_e \varepsilon_0}{e^2} = \frac{1.12}{\lambda_0^2[\mu\text{m}]} \quad [10^{21}\text{cm}^{-3}], \tag{2.23}$$

which gives the threshold number density at which total reflection occurs. $\lambda_0 = 2\pi\omega_0$ is the fundamental frequency of the laser. The earlier limits can thus be reformulated in terms of plasma number density instead. When $n_e > n_c$, the plasma is said to be overdense, and the laser pulse is not transmitted. When $n_e < n_c$ it is underdense, and the laser may propagate through the plasma. As an example, with the laser used in this project, which has a wavelength of 0.8 μm, the critical density is $1.75{\cdot}10^{21}$ cm^{-3}.

The group and phase velocity of an electromagnetic wave are defined as [12, 14]:

$$v_{ph} = \frac{\omega_0}{k}, \qquad v_g = \left(\frac{dk}{d\omega_0}\right)^{-1}. \tag{2.24}$$

Therefore, by using Eq. (2.21) and then Eq. (2.22), the v_{ph} and v_g of the electromagnetic wave in the plasma are:

$$\begin{aligned} v_{ph} =& \sqrt{c^2 + \frac{\omega_p^2}{k^2}} = \frac{c}{\sqrt{1 - \frac{\omega_p^2}{\omega_0^2}}} \\ v_g =& \frac{c^2}{v_{ph}} = c\sqrt{1 - \frac{\omega_p^2}{\omega_0^2}}. \end{aligned} \tag{2.25}$$

Since $\omega_0 > \omega_p$ was the condition for laser propagation through the plasma, the phase velocity of the electromagnetic wave in the plasma is greater than c. Consequently, the group velocity is always less than c. However, for a driving laser pulse that does not evolve significantly in the plasma, $v_{ph} \simeq v_g$, the normalized phase velocity, β_p and the relativistic factor of the plasma γ_p are:

$$\begin{aligned} \beta_p &= \frac{v_g}{c} = \sqrt{1 - \frac{n_e}{n_c}} \\ \gamma_p &= \frac{1}{\sqrt{1 - \beta_p^2}} = \sqrt{\frac{n_c}{n_e}}. \end{aligned} \tag{2.26}$$

It can thus be observed that a smaller ratio between the plasma density and the critical density, n_e/n_c, leads to a higher β_p and a greater γ_p. In principle, by decreasing n_e, the phase velocity of the plasma can be increased.

2.3.2 Self-focusing

As the laser propagates in the plasma, it will be modulated, and for this project, self-focusing is of particular interest, since it changes the transverse size of the laser during its propagation. As will be seen, this will affect the bubble which electrons can be accelerated in, described in more detail in section 3.2.

For a certain laser intensity, the relativistic nonlinear regime will be reached. The spatial variation of the laser pulse intensity will cause a variation of the plasma's refractive index. Consequently, the variation in the plasma density's spatial refractive index will cause the plasma to act as a focusing lens. The mechanism is called self-focusing. In this scenario, the laser's diffraction can be precisely balanced and the laser can propagate self-consistently. The spatial index of refraction of the plasma can be expressed as $\eta(r) = c/v_{ph}$. Inserting the v_{ph} defined in Eq. (2.25), and assuming a uniform plasma density, as well as a large amplitude plasma wave, the following expression is obtained [11, 16]:

$$\eta(r) = \left(1 - \frac{\omega_p^2(r)}{\omega_0^2}\right)^{1/2} \simeq 1 - \frac{1}{2}\frac{n_e(r)}{\gamma(r) n_c}, \tag{2.27}$$

which can be expanded as:

$$\eta(r) \approx 1 - \frac{\omega_p^2}{2\omega_0^2}\left(1 - \frac{a^2}{2} + \frac{\delta n_e}{n_0}\right). \tag{2.28}$$

where n_0 is the background plasma density. In the expression, $a^2/2$ corresponds to the relativistic guiding of the laser, and $\delta n_e/n_0$ the plasma waveguiding, self-channeling and the self-modulation of long pulses [17]. It can thus be observed that modulation of the refractive index that leads to self-focusing scales with a^2, and the change in n_e, hence, there is a threshold minumum laser power that will lead to the balancing of the diffraction, called the critical laser power [17]:

$$P_c = 17\frac{\omega_0^2}{\omega_p^2} \quad [\text{GW}]. \tag{2.29}$$

When the laser power is such that $P/P_c > 1$, the laser propagation is dominated by relativistic self-guiding [16].

3

Laser wakefield acceleration

Tajima and Dawson showed through theory and numerical analysis that a laser of high power density, 10^{18} W/cm^2, could generate an electric field of 10^9 V/cm^2 [4], from which electrons could be accelerated to a high energy over a short distance. They proposed two schemes for the acceleration, called the beat wave and the laser wakefield, and common for both is that an intense laser excites a wave in the plasma. In the 1990s, several experiments followed from their work, where electrons of a few MeV where injected and accelerated in a field of the GV/m range [18]. The development of the chirped-pulse amplification (CPA) laser system, pioneered by Strickland and Mourou [19], led to consequently more powerful laser systems, and it was possible to accelerate the electrons in fields to more than one TV/m. The laser wakefield had one great breakthrough in 1994, when a group at Rutheford Appleton Laboratory demonstrated the self-modulated laser wakefield [18, 20]. The amplitude of the plasma wave was so large that electrons could be trapped and accelerated with the laser. These first electron beams had a broad energy distribution due to the random process of the injection, and did not compare well to what was obtainable by conventional accelerators [18]. In order to control the shape of the electrons, it is needed that the injected electrons has a duration much smaller than the excited plasma wave period, much less than 10 fs, which was done in 2004 by three independent groups [21, 22, 23]. It was also shown that the distribution and shape of the electron pulses is dependent on the density of the plasma [23]. Moreover, they produced quasi-monoenergetic electron beams, demonstrating the bubble regime. The electron pulses had high quality as a result of controlling the laser plasma parameters, better diagnostic techniques, and extension of the laser's propagation in the plasma. Also, a better understanding of the underlying physics of the plasma and laser interaction, in particular the importance of matching the laser parameters to the plasma. For one, efficient acceleration is obtained if the acceleration length is matched to the dephasing lenght, which can be thought of as the length for which the electrons outrun the laser [3].

3.1 The ponderomotive force

A charged particle, moving in the inhomogeneous field of an electromagnetic wave will experience a time-averaged force which acts to push the electrons away from the regions of high gradients in the laser intensity. This is called the ponderomotive force [11]. Recalling Eq. (2.13), the second term of the right hand side $\mathbf{v} \times \mathbf{B}$ describes the nonlinear excitation of a plasma wave, and it is also responsible for the ponderomotive force.

In the nonlinear regime, the electron both oscillates in the longitudinal and transverse direction, and in the latter, the electron has a velocity $\mathbf{v_q}$, called the quiver velocity [3]. The momentum in this direction then can be expressed as $\mathbf{p_q} = \gamma m_e \mathbf{v_q}$. One way to obtain an expression for the nonlinear ponderomotive force is by starting from the linear regime. In the linear regime, $a_0 \ll 1$, the electron oscillates predominantly in the transverse direction, and the longitudinal oscillation can be treated as a perturbation. The total momentum thus becomes $\mathbf{p} = \mathbf{p_q} + \delta\mathbf{p}$. Inserting this, together with the vector potential description of the electromagnetic field in Eq. (2.9), into the Lorentz equation, Eq. (2.13) and using the identity $d/dt = \partial/\partial t + \mathbf{v}\nabla$, yields the second order motion [3]:

$$\frac{d\delta\mathbf{p}}{dt} = -m_e c^2 \nabla \langle a^2 \rangle. \tag{3.1}$$

In the linear regime, the ponderomotive force is given by the above expression, averaged over the fast laser field oscillation:

$$\mathbf{F_p} = -m_e c^2 \frac{\nabla \langle a^2 \rangle}{2}. \tag{3.2}$$

To obtain the ponderomotive force in the 3D nonlinear regime, this expression has to be adjusted. For a collisionless plasma, the nonlinear ponderomotive force becomes [24]:

$$\mathbf{F}_{\mathbf{p}NL} = -m_e c^2 \nabla \langle \gamma \rangle, \tag{3.3}$$

where $\langle \gamma \rangle$ is the slow variation of the relativistic factor, averaged over the fast laser period [3, 15]. The expression is independent of the polarization of the laser, and it is this force that the LWFA relies on.

3.2 The bubble regime

The LWFA scheme, exploits the nonlinear ponderomotive force. As can be seen in Eq. (3.3), $\mathbf{F}_{\mathbf{p}NL}$ relies on the particle mass. Therefore, when a plasma is subjected to a non-uniform laser pulse of high intensity, the electrons will experience a stronger force from the laser than the much heavier ions. Due to this strong force, the electrons will be pushed away from the laser's focus, creating a "wake" behind

the laser that is almost completely evacuated of electrons. In this cavity, or *bubble*, the accelerating field can be of the order of hundreds of GV/m [2]. The injected electrons, i.e. the electrons that has successfully entered the bubble, such that they co-propagate with the laser, are highly relativistic and travels with a velocity close to the laser's group velocity [2]. An example of the bubble and the electric field along it can be seen in Fig. 3.1. where the electrons have accumulated at the back. There, the electric field is negative, while at the front, behind the laser, it is positive. On axis, the electric field is zero. The figure shows a snapshot of the LWFA, and the lighter gray area surrounding the bubble shows the background electrons of the plasma. It can be seen that at the back of the bubble, that electrons have accumulated, while the whiter area in the bubble shows the absence of electrons. The laser pulse is propagating from left to right in the figure and is not directly plotted but the effect of it can be seen as the wave pattern around the position $z = 113$ µm.

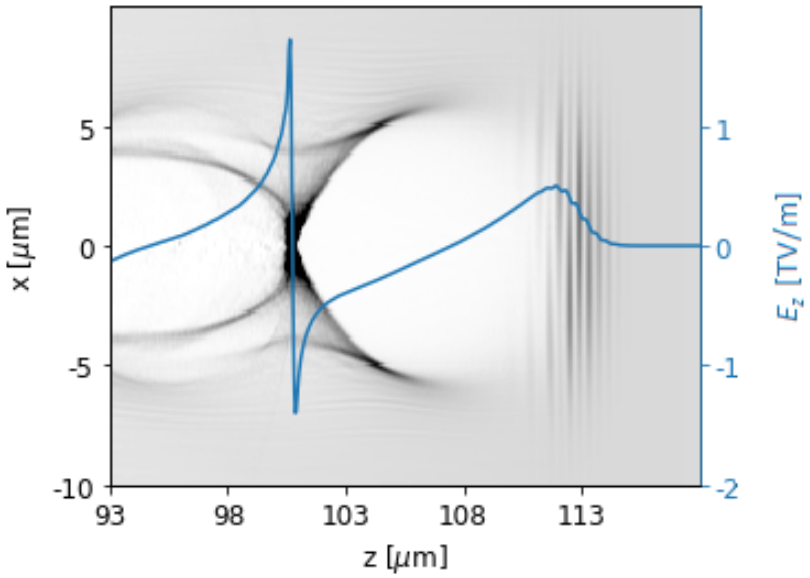

Fig. 3.1: *Snapshot of the charge density, ρ, from an FBPIC simulation, illustrating the bubble regime. For the simulation, the laser intensity corresponds to $a_0 = 3.4$, an electron density of $n_e = 1 \cdot 10^{19}$ cm^{-3}, laser FWHM pulse duration of $\tau_0 = 7$ fs, and a beam waist of $w_0 = 6.2$ µm. The blue line shows the electric field in the z-direction.*

For an efficient guiding of the laser in the bubble regime, the waist of the laser must be matched to the intensity. For intensities corresponding to a normalized vector amplitude $a_0 \gtrsim 2$, Lu et al. have through simulations phenomenologically showed that the matching condition is [16]:

$$k_p w_0 = 2\sqrt{a_0}, \tag{3.4}$$

where $k_p = \omega_p / v_{ph}$ is the wavenumber of the plasma wave. The radius of the bubble can be described by $k_p R \simeq k_p w_0$, which then means that:

$$R \simeq w_0 = 2\sqrt{a_0}/k_p. \tag{3.5}$$

The magnitude of R varies depending on the intensity of the laser and the plasma number density. From Eq. (3.5), it is evident from that the size of the bubble scales with $n_e^{-1/2}$. Therefore, if the number density of the plasma is modulated, so is the size of the bubble.

The expelled electrons follows a collective motion which leads to the formation of the bubble seen Fig. 3.1. Electrons that manage to escape it can then enter the cavity, i.e., they can be *injected*, and thus accelerated and the maximum accelerating electric field can be estimated from the Poisson relation:

$$\nabla \cdot \mathbf{E} = -e(n_e - n_0). \tag{3.6}$$

By assuming that the plasma electrons are oscillating with $k_p = \omega_p/c$, two solutions are obtained; $(\omega_p/c)E_{max} = en_0$ and $E_{max} = E_0$, where:

$$E_0 = \frac{m_e c\omega_p}{e} \simeq (96 \text{ GV/m})\sqrt{n_e \, [10^{18} \text{ cm}^{-3}]}, \tag{3.7}$$

is the cold, non-relativistic wavebreaking field [3]. However, in the nonlinear regime, it is possible for the maximum electrical field to exceed E_0.

3.3 Dephasing and pump depletion length

In the nonlinear regime, there are two length of importance that determines the particle energy gain of the accelerated electrons; the pump depletion length, L_{pd}, defined as the distance for which half of the laser energy has been transferred to the plasma wave, and the dephasing length, L_d, which is the distance the electrons that has entered the bubble outrun the laser and starts to decelerate. These two effects are intrinsic to the laser-plasma acceleration and depend on both the laser intensity and the electron density [3, 16].

The pump depletion length, L_{pd}, can be thought of as the length over which the laser can sustain the excited wake, and is in the bubble regime estimated via the etching velocity [14]:

$$v_{etch} \simeq \frac{c\omega_p^2}{\omega_0^2}, \tag{3.8}$$

which in turn describes erosion velocity of the laser front the moment before it starts self-focusing. For a laser with a pulse length of τ_0 and an etching velocity as described above, the L_{pd} becomes:

$$L_{pd} = \frac{c}{v_{etch}} c\tau_0 = \frac{\omega_0^2}{\omega_p^2} c\tau_0. \tag{3.9}$$

The dephasning length, L_d, on the other hand, depend on the modification of phase velocity of the plasma wave, which in the 3D nonlinear regime is $\beta_p = 1 - 3\omega_p^2/(2\omega_0^2)$. Therefore, for a bubble with a radius of R, the L_d can be expressed as:

$$L_d = \frac{R}{1-\beta_p} \simeq \frac{2}{3}\frac{\omega_0^2}{\omega_p^2} R = \frac{4}{3}\frac{\omega_0^2}{\omega_p^2}\frac{\sqrt{a_0}}{k_p}. \tag{3.10}$$

A criterion for effective electron acceleration is matching the electron density for a given laser amplitude such that $L_{pd} \approx L_d$, which gives the following relation:

$$2\frac{\sqrt{a_0}}{k_p} = R \approx \frac{3}{2} c\tau_0, \tag{3.11}$$

which means that if the matching criterion is met, then the bubble radius is approximately 3/2 of the laser's pulse length. A pulse with a duration of 7 fs would then correspond to a bubble radius of approximately 3.1 µm, hence, the required laser beam waist for an effective acceleration is $w_0 = 3.1$ µm. When self-focusing occurs, w_0 will decrease, and consequently the radius of the bubble. The dephasing and pump depletion length dependency on the electron density can be seen in Fig. 3.2 for a laser intensity corresponding to $a_0 = 3.4$. From the figure it can be observed that the optimum density is approximately $4{\cdot}10^{19}$ cm^{-3} giving $L_{pd} \approx L_d \approx 90$ µm.

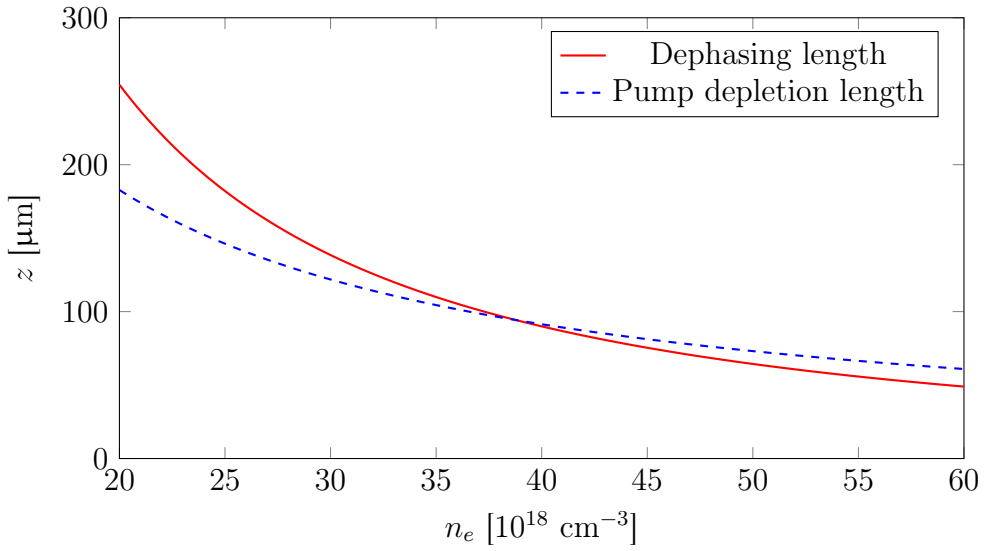

Fig. 3.2: *Pump depletion length, L_{pd} and the dephasing length L_d calculated and plotted for different electron densities, n_e. The laser has an intensity corresponding to $a_0 = 3.4$ and a FWHM duration of 7 fs, which also is used in the simulations.*

3.3.1 The energy gain of the electrons

As the electrons are accelerating in the plasma wave, their energy gain be descried by [14, 16]:

$$\Delta W = eE_z L_{acc} \tag{3.12}$$

where E_z is the accelerating field associated with the plasma wave, and L_{acc} the distance for which the electron is submitted to the field. Since the bubble is roughly a sphere with radius R, and if the electrons are injected at at the back of the bubble, the electrons then travel a relative distance of R before they dephase. This leads to a peak useful acceleration field of $eE_{z,max}/(mc\omega_p) = \sqrt{a_0}$. The field is roughly linear, leading to the average field being half of the maximum field, $eE_{z,max}/(mc\omega_p) = \sqrt{a_0}/2$. Also, it is desired that $L_{acc} \approx L_d$, since this gives the longest acceleration length before the electrons starts to decelerate [16], and in 2004, it was shown that when $L_{acc} \approx L_d$, low energy spread electrons were produced [21, 22, 23]. Thus, insertion of the expression of the average field together with (3.10) in (3.12) gives:

$$\Delta W \simeq \frac{2}{3}\frac{\omega_0^2}{\omega_p^2} a_0 m_e c^2 \simeq \left(\frac{e^2 P}{m_e^2 c^5}\right)^{1/3} \left(\frac{n_c}{n_e}\right)^{2/3} m_e c^2. \tag{3.13}$$

And in practical units, this can be expressed as:

$$\Delta W \simeq 1.7 \left(\frac{P[\mathrm{TW}]}{100}\right)^{1/3} \left(\frac{0.8}{\lambda_0[\mu\mathrm{m}]}\right)^{4/3} \left(\frac{1}{n_e[10^{18}\mathrm{cm}^{-3}]}\right)^{2/3} \quad [\mathrm{GeV}]. \tag{3.14}$$

Thus, the energy gain of the accelerated electrons can essentially be tuned by adjusting the laser power, thus affecting a_0, but more effectively by changing the electron density, n_e.

3.4 LWFA scaling laws

Summarizing the equation given so far, phenomenological scaling laws, given by Lu et al. for a matched LWFA can be obtained. In table 3.1, the ones presented in this chapter, which is valid for a 3D nonlinear regime are given for a laser intensity corresponding to $a_0 > 2$.

Table 3.1: *Scaling laws for the 3D nonlinear regime, developed from [16].*

a_0	w_0	L_d	L_{pd}	γ_p	$\Delta W/m_e c^2$
>2	$\frac{2\sqrt{a_0}}{k_p}$	$\frac{4}{3}\frac{\omega_0^2}{\omega_p^2}\frac{\sqrt{a_0}}{k_p}$	$\frac{\omega_0^2}{\omega_p^2} c\tau_0$	$\frac{1}{\sqrt{3}}\frac{\omega_0}{\omega_p}$	$\frac{2}{3}\frac{\omega_0^2}{\omega_p^2} a_0$

These scaling laws assume a non-evolving laser intensity, which is not true once the nonlinear regime is reached. Also, the parameters are not fully valid once the electrons becomes relativistic. However, they act as a guideline in an experimental

setup, and are also used as a guideline throughout this project when evaluating the simulation results.

3.5 Electron injection

For the electrons to be accelerated, they must be injected to the cavity, or bubble, behind the laser in order to be subjected to the electric field gradient. Here, *self-injection* and *density down-ramp injection* will be explained.

3.5.1 Self-injection

To achieve self-injection, the laser intensity is increased until the ponderomotive force causes so large oscillations by the electrons that they escape the collective motion that creates the wake and breaks the wave. Recalling from Eq. (2.28), the plasma can act as a focusing lens as the laser propagates through it. As the laser pulse self-focuses, the intensity will increase. These electrons can be injected and trapped behind the laser pulse, and the trapping stops when the charge of the injected bunch compensates for the ionic charge. As long as the intensity of the laser is high enough, the structure remains stable [18]. For an optimal acceleration of the particles, the intensity has to be chosen such that the corresponding a_0 fulfills the matching condition in Eq. (3.4), which also sets a condition on n_e for which the plasma can sustain the self-guiding effect. In order for the electrons to break the wave during the first plasma wave period, the laser requires an electric field [25]:

$$\frac{E_{WB}}{E_0} = \sqrt{2(\gamma_p - 1)}, \tag{3.15}$$

where the subscript WB denotes "Wave Breaking", and E_{WB} is the cold *relativistic* 1D wavebreaking field. The expression is valid for low temperature, plane plasma waves. In the highly relativistic regime, when the laser pulse duration is shorter than the plasma period, and when the intensity is high enough, such that the nonlinear regime is entered, then the wave front is curved. The wave then breaks closer to the propagation axis, leading to a lower required electric field strength than in Eq. (3.15). However, when the electric field strength exceeds the wave breaking limit, a larger amount of electrons may be trapped in the cavity behind the driving laser [25].

Even though self-injection is experimentally easy to implement, the lack of controlled injection and reproducibility has led to the development of other injection mechanisms, such as the density down-ramp injection.

3.5.2 Density down-ramp injection

The density down-ramp injection exploits the plasma wavelength dependence on the plasma density, and by creating a gradient in the density profile, as seen in Fig. 3.3,

controlled injection of electrons can be done. In Fig. 3.3, a peak region and plateau region is created, denoted by I and II in the figure. The two regions are then joined by a negative gradient for which injection of electrons can occur. This method was introduced by Bulanov et al. [5], in particular a slow transition between the two regions were explored. Later, Suk et al. [26] investigated the down-ramp with a sharper transition between the density regions. Common for the schemes in Ref. [5] and [26] is that the electrons after the injection are accelerated over the plateau region, i.e. region II. The length of the down-ramp region, L_{dr} affects the beam-loading effect which is the injected eletrons' influence on the electric field within the bubble. L_{dr} also determines the sharpness in transition between the two regions. Experimentally the density regions could for example be obtained by using two orthogonal gas-nozzles, both of which are orthogonal to the propagation axis of the laser. The method was exploited at Lund Laser Center [6], and it was shown that the accelerating field could be controlled by adjusting the number density in region I. In comparison to self-injection, the density down-ramp injection has proven to be reproducible. As an example, in [6], the accelerated electrons had a measured charge of 1 pC, with a shot-to-shot standard deviation of 13 %, and in energy it was 5 %. While the self-injected electrons had a charge of 30 pC, but a standard deviation of 50 % and limited reproducibility.

When the laser propagates over the negative density gradient, the phase velocity of the bubble will gradually decrease until it becomes equal to the plasma fluid oscillation. This causes the wave to break, and hence, electrons are injected and trapped in the desired plasma wave period [5, 26]. Typically, the plateau number density, n_e, is well below the matched density for an optimum LWFA, while in a self-injection scheme the matched density is preferable. This is because in the former, it is desirable to avoid injection due to mechanisms other than the change in the density profile. As a consequence, a controlled and localized injection occur in the gradient [5, 6, 7, 26].

The scaling law presented in Eq. (3.4), which applies to the matched regime, is no longer applicable [7]. In a down-ramp scheme, the laser intensity cannot be matched to both of the density regions at the same time, thus the scaling laws do not apply throughout the whole density profile. Due to the highly relativistic and nonlinearity of the bubble regime, theoretical analysis are difficult to establish. However, parametric studies of the down-ramp region has shown that the injected electron bunch length can be predicted from numerical simulations as [7]:

$$L_e = C_1 \Delta\lambda_p + C_2 Q^2 \tag{3.16}$$

where C_1 and C_2 are constants determined numerically, and $\lambda_p = 2\pi c/\omega_p$ is the plasma wavelength. Q is the total charge of the injected electron bunch. The constant C_1 couples the linear non-relativistic theory to the true plasma wavelength, λ_p, and is dimensionless. It takes into account the plasma wavelength dependence on the laser intensity, a_0. The first term on the right hand side, $C_1\Delta\lambda_p$, gives the true plasma wavelength difference between the two regions in Fig. 3.3, without the beamloading effect. C_2 has the dimension *length/charge*^{2}, and together with

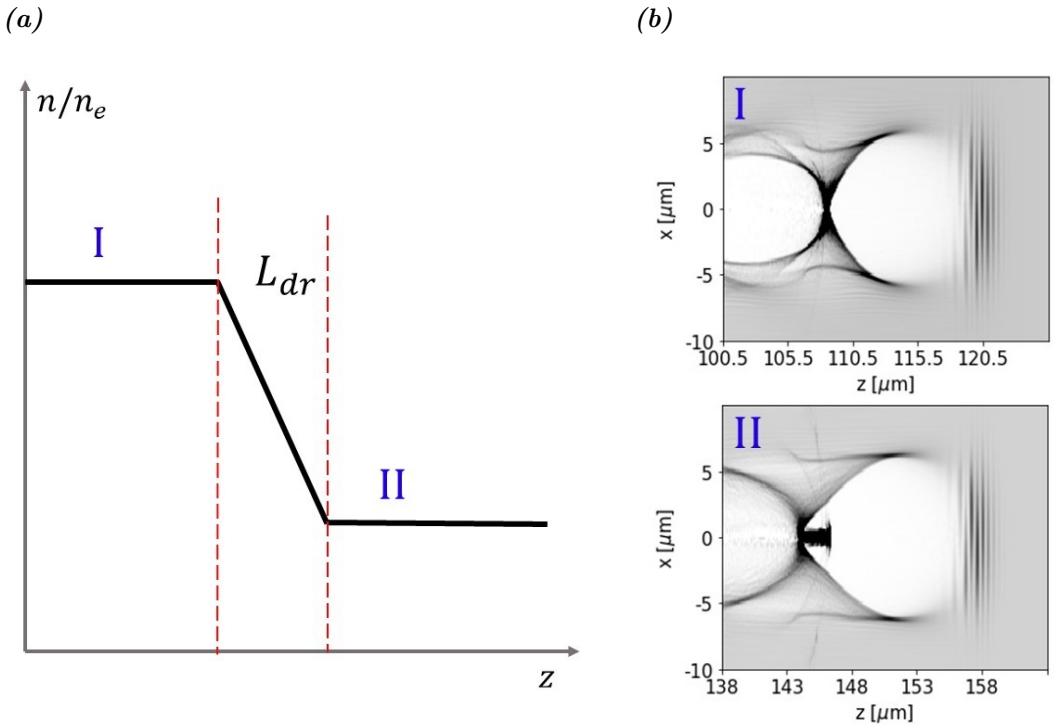

Fig. 3.3: *(a)An illustration of the density profile utilized in a density down-ramp scheme. Injection happens in the down-ramp region, between region I and II. (b) The bubble before and after the gradient, aqcuired from FBPIC simulations, explained in section 4.4. In region II, the bubble has expanded, and electrons have been injected.*

Q, the second term on the right hand side of Eq. (3.16) describes the elongation of the bubble due to the beamloading effects. By numerically simulating the required parameters, C_1 and C_2 can then be fitted to the datapoints, leading to a predictive model for a specific setup [7]. It was also shown in [7] the influence of the gradient steepness in terms of the injection process. For a steep transition, the injection process becomes more complicated in comparison with a gentler transition. The injected electrons experience an abrupt change of the bubble radius, which also causes large oscillations once the the electrons are trapped. For the gentler gradient, the electrons propagates along the sheath before they accumulate at the rear of the bubble, from which they are injected.

Density modulation

Tooley et al. [2] proposed an LWFA scheme exploiting arbitrary variation of the plasma density profile which led to controlled injection of electrons in the bubble regime. The density profile can be seen in Fig. 4.4, in section 4.5.1 of this report. Similarly to the setup used in [6], the simulated profile corresponds to an experimental setup with two orthogonal gas-nozzles which in turn are orthogonal to the laser's propagation direction.

The density profile in [2] causes the expelled electrons to propagate along the sheath before they are injected to the bubble, similarly to the slow gradient trapping described in [7]. In their case, w_0 is matched to n_e in order to minimize the evolution of a_0 due to self-focusing as the laser propagates through the plasma. Over the down-ramp region, the phase velocity of the back of the bubble β_p decreases, and hence injection occurs [27], much similar to the linear down-ramp density in Fig. 3.3. Before the decrease in density, and before region I in Fig. 3.3, the scheme in [2] has a positive gradient. Over this positive gradient, self-injection is completely suppressed if β_p is increased such that it exceeds unity [27].

The in-homogeneity of the density profile described in [2], is also used in this project, and given in the input script for the FBPIC algorithm. Mathematically, slightly modified from [2], the plasma number density inhomogeneity can be described by:

$$\frac{n}{n_e} = \begin{cases} h(z)z/L_r & \text{if } z \leq L_r \\ 1 + h(b - |z - z_i|)\alpha \cos^2(\pi \frac{z - z_i}{2b}) & \text{if } z \geq L_r, \end{cases} \tag{3.17}$$

where $h(z)$ is the Heavyside function, L_r the initial ramp length of the plasma, z_i the position of the peak density with half-width b. In [2], the duration of the electron bunches from the simulation using this injection mechanism, has a shortest duration just below one fs. However, in their simulations, the laser has an intensity corresponding to $a_0 = 4$, thus being more intense than the laser used in the simulations performed in this project, presented in section 4.5.

4

Particle in cell simulations

A computational simulation acts as complement to physical experiments and theoretical models. Through the growth of commercially available computers, it has become widely used as a tool to test or perform experiments where diagnosis in a physical experiment perturbs the measurement [8, 9]. For LWFA experiment, numerical simulations help with the understanding of the underlying physics, where the models often are complex due to the highly relativistic and nonlinear interaction between the laser pulse and the plasma. Commonly, a PIC-code is used for simulations of LWFA, and here in this projected FBPIC is used, which is suitable for close to cylindrical geometries, which an ideal LWFA fulfills [10].

In a PIC, or in early works, a cloud in cell (CIC) algorithm, the physical particles are bunched together and represented by a finite number of macroparticles [8, 9]. To obtain the field, the Maxwell's equations are solved by a discretized finite difference method, i.e., the fields are solved on a spatial grid, and the charge is then obtained from the particles [9]. This reduces the computational cost in comparison to if the Columb interaction between N particles is computed, which gives a summation over N^i interactions, where i denotes the number of dimensions. To fully resolve the physics observed, the number of macroparticles must be sufficient, such that the macroscopic behavior represents the microscopic. If too few are chosen, then discrete particle effects occur, such as exaggeration of the fluctuations and collisions (the latter not of any significant interest here) [9]. However, the discretization of the fields may also lead to numerical errors, such as spurious numerical dispersion in the propagation of the electromagnetic wave, which in this context means that unphysical effects may be computed. As will be explained below, the FBPIC-code avoids this problem, but first the general PIC algorithm will be explained.

4.1 The kinetic equation

The kinetics of the particles of the laser-plasma interaction can be described by the general equation:

$$\frac{\partial f}{\partial t} + \frac{\mathbf{p}}{\gamma m_e}\nabla_{\mathbf{r}} f + q\left(\mathbf{E} + \frac{\mathbf{p}\times\mathbf{B}}{\gamma m_e}\right)\nabla_{\mathbf{p}} f = C(f) + \zeta(f), \tag{4.1}$$

where f is the single particle distribution function, $\mathbf{p}$ the momentum, $\mathbf{E}$ and $\mathbf{B}$ the electric and magnetic field respectively. On the right hand side, $C(f)$ is the collision operator while $\zeta(f)$ is a potential source term, that is present if ionization/recombination processes occur [28]. However, for a fully ionized and collisionless plasma, as is considered here, both $C(f)$ and $\zeta(f)$ can be neglected and (4.1) takes the form of the Vlaslov equation. This equation must be coupled to the Maxwell's equations, or rather, two of them:

$$\begin{aligned}\frac{\partial \mathbf{E}}{\partial t} &= -\frac{\mathbf{j}}{\varepsilon_0} + c^2\nabla\times\mathbf{B}\\ \frac{\partial \mathbf{B}}{\partial t} &= -\nabla\times\mathbf{E},\end{aligned} \tag{4.2}$$

where $\mathbf{j}$ is the current density, and here also the source term. It can be obtained by solving the first moment, i.e. the expected value or mean of the distribution function, f. These equation together therefore forms a closed set. One approach is to directly solve Eq. (4.1), by finite differentiation. However, if N grid points are used in each dimension, the needed storage scales as N^i. The direct finite difference approach therefore quickly becomes computationally expensive, if one seeks to solve the equation in more than one dimension [28].

4.2 Particle approach

The above described problem can be reduced by defining the charges as a finite set of *cloud* charges or as *macroparticles* to represent the distribution function. In comparison to charged particles, that experience a Coulomb force between them, the overall force for a charge cloud, or macroparticle is *Coulombic*. Meaning that instead of two particles experiencing a strong force at short distance from each other r, that exponentially decays, the macroparticles at a short distance from each other experience a force that goes toward zero. While at a long distance from each other, the overall force is the Coulomb force experienced between two single particles. This allows the macroparticles to pass through each other, appearing collisionless and hence reducing required computational power [8]. The distribution function can thus be written as a sum of all macroparticles as:

$$f = \sum_i g_i(\mathbf{r} - \mathbf{r}_i(t), \mathbf{p} - \mathbf{p}_i(t)). \tag{4.3}$$

where $g_i(\cdot)$ describes the size and momentum of the i-th macroparticle. Substituting this into Eq. (4.1), and using the chain rule, the two functions emerge:

$$\begin{aligned} \frac{d\mathbf{r}_i}{dt} &= \frac{\mathbf{p}_i}{\gamma_i m_i} \\ \frac{d\mathbf{p}_i}{dt} &= q_i(\mathbf{E} + \mathbf{v}_i \times \mathbf{B}). \end{aligned} \tag{4.4}$$

Thus, the macroparticles can be evolved as a set of single particles, and this approximation is a fully consistent approach to the Vlaslov-Maxwell equation system [28].

The algorithm now works such that field are defined on a discrete grid, meaning that the Maxwell's equations are solved on the grid for which the macroparticles moves through. The macroparticles are interpolated onto the grid to obtain current densities, and the electric- and magnetic field are interpolated from the grid to obtain these at each macroparticle [8]. A simple schematic of the procedure of a PIC-algorithm can be seen in Fig. 4.1.

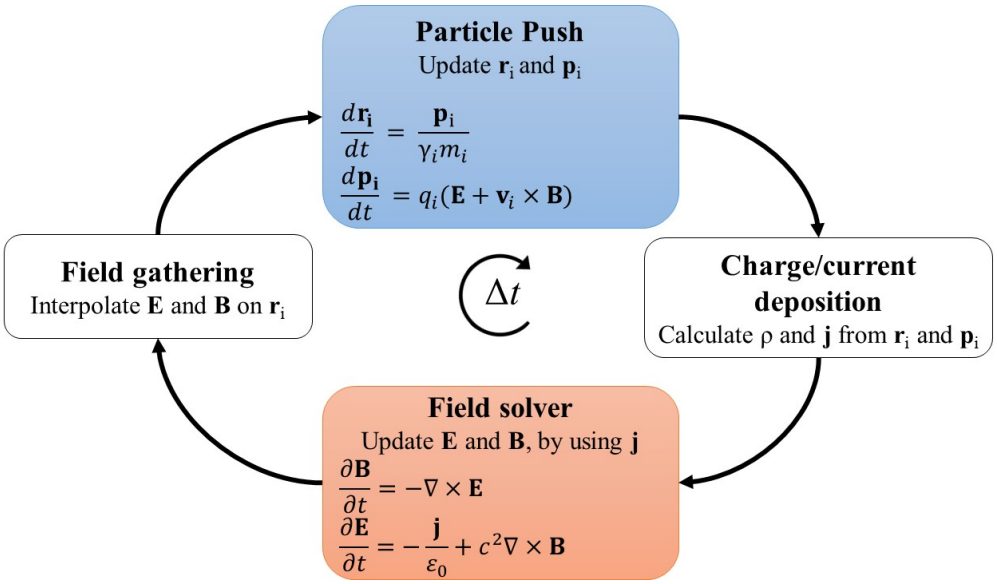

Fig. 4.1: *Schematic showing the interpolation that is done at each iteration (timestep). Image adapted from [29].*

4.3 Particle pusher and interpolation

Particle pusher refers to the update of the momentum and position of the macroparticle. The way this is done depends on the numerical method chosen as the solver of the differential equation described in previous section. The simplest particle pusher is that of the position, and if the Leapfrog method is used, then the update in one spatial dimension for a macroparticle at the $(n+1)$-th timestep is [28]:

$$\frac{x^{n+1} - x^n}{\Delta t} = \frac{p_x^{n+1/2}}{\gamma^{n+1/2} m}. \tag{4.5}$$

The update of the momentum, in three-dimensions, is most effectively done by using the *Boris method* instead of the Leapfrog method. This is due to the complexity the term $\mathbf{v} \times \mathbf{B}$ adds to the equation. However, separating the effect of $\mathbf{E}$ and the rotation in Eq. (4.4), then the first step of the Boris method is accelerating the particle in the $\mathbf{E}$-field for half a timestep:

$$\mathbf{p}^{-} = \mathbf{p}^{n-1/2} + q\mathbf{E}^{n}\frac{\Delta t}{2}. \tag{4.6}$$

where $\mathbf{p}^{-}$ corresponds to $\mathbf{p}$ for a decreasing iteration step, $-1/2$. Next, the rotation $\mathbf{v} \times \mathbf{B}$ is performed to obtain $\mathbf{p}^{+}$, which is the current $\mathbf{p}$ at a increasing iteration step $+1/2$. Throughout this step, γ is constant, which is denoted by γ', and the equation may be written as [28]:

$$\frac{\mathbf{p}^{+} - \mathbf{p}^{-}}{\Delta t} = \frac{q}{2\gamma' m_e}(\mathbf{p}^{+} + \mathbf{p}^{-}) \times \mathbf{B}^{n}. \tag{4.7}$$

The last step of the particle push is once again accelerating the macroparticle in the electric field for half a timestep. Note here the positive sign in the step taken.

$$\mathbf{p}^{+} = \mathbf{p}^{n+1/2} - q\mathbf{E}^{n}\frac{\Delta t}{2}. \tag{4.8}$$

To obtain the grid charge of a particle and the force from the electric field, an appropriate interpolation has to be done. This is done by a particle-grid interpolation, which depends on the i-th macroparticle and the j-th spatial cell as [9]:

$$\rho_j \equiv \rho(X_j) = \sum_i q_i S(X_j - x_i), \tag{4.9}$$

$$\mathbf{F}_i = q_i \Delta x \sum_j \mathbf{E}_j S(X_j - x_i), \tag{4.10}$$

where $S(\cdot)$ is a weight function, which describes the shape of the marcroparticle. The $S(\cdot)$ in (4.9) and (4.10) does not have to be of the same shape, but usually is to avoid gravitation-like instability, i.e., the macroparticle exerting a force on itself. Usually, $S(\cdot)$ is isotropic and uniform [9]. Moreover, if it is isotropic, then it is also real valued. A simple zeroth order interpolation uses an area weighting method, which is called the nearest grid point (NGP) method, which is illustrated in Fig. 4.2. The red box illustrates an arbitrary finite-sized macroparticle with a center point at c, located somewhere on the grid, illustrated by the heavy black lines. The size of the particle is, for simplicity of this example, the same as one defined grid cell, or just cell. The dashed lines shows a grid with gridpoints at the center of the heavy dashed lines, and the intersection of the dashed lines with the macroparticle divides it into four areas, A_1, A_2, A_3 and A_4. Each gridpoint, 1, 2, 3, and 4, is now assigned a charge. For simplicity of the example, let $\Delta x = \Delta y$, then gridpoint 1 gets assigned a charge of $qA_1/\Delta x^2$, and 2 $qA_2/\Delta x^2$ and so forth. These assigned charges now have the same dipole moment with respect to each dashed grid-line as the original particle have [8]. This describes a uniform charge cloud. What is also a common

interpolation method, and made similarly to NGP is the first order weighting called the CIC method, or as it also is called, the PIC method. The difference between the NPG and CIC shape functions are illustrated in Fig. 4.3. Even higher order weighting can be used, but the increasing order also leads to increased complexity of the code [9]. On the other hand, higher order interpolations improves the accuracy, smoothness, among others, e.g. energy conservation [28].

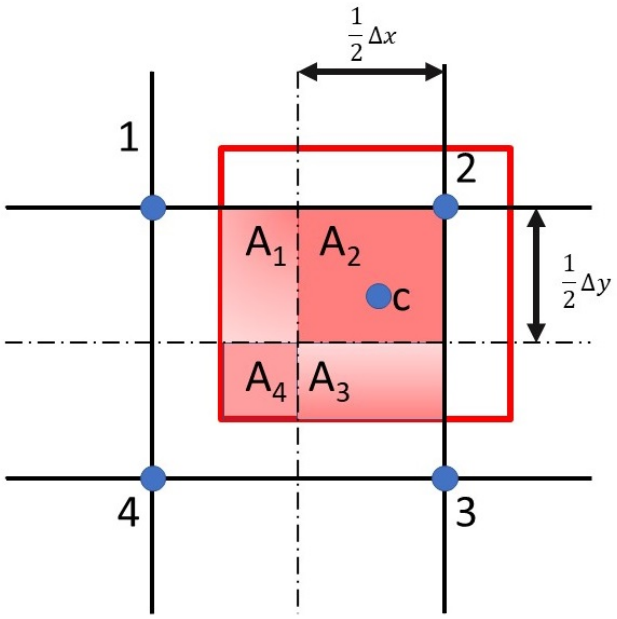

Fig. 4.2: *An illustration of the NGP method, or as it also is called, area-weighting method. Image developed from [8, 9].*

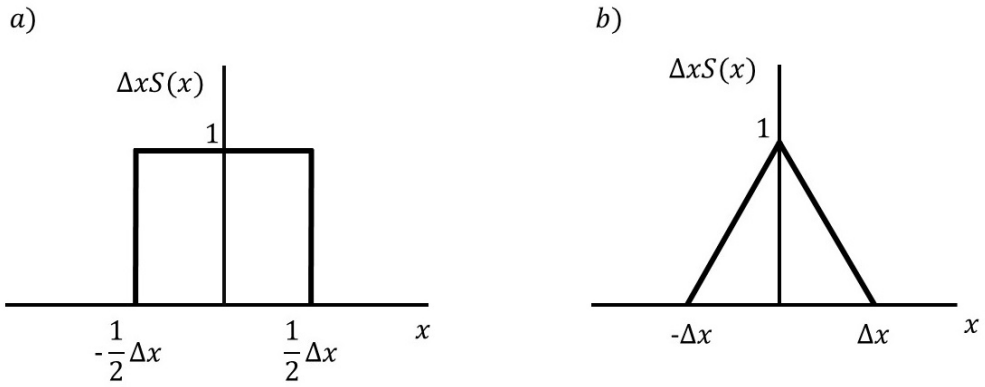

Fig. 4.3: *Illustration of a) zeroth order shape function (NGP) and b) first order shape function (CIC, PIC). Image developed from [9].*

For a linear shape function, in one dimension, the macroparticle will contribute to the charge density in two points only, such as [10, 28]:

$$\rho_j = q_i \frac{x_{j+1} - x_i}{\Delta x} \quad \text{and} \quad \rho_{j+1} = q_i \frac{x_i - x_j}{\Delta x}. \tag{4.11}$$

Hence, only two gridpoints contributes to the electric field:

$$E_{x,i} = E_{x,j}\frac{x_{j+1} - x_i}{\Delta x} + E_{x,j+1}\frac{x_i - x_j}{\Delta x}. \tag{4.12}$$

The interpolation scheme is conceptually the same in two- and three dimensions and can therefore easily be adapted. Moreover, the particle grid interpolation is a crucial step in the PIC algorithm, and it is where most of the non-physical behaviors emerge.

4.4 Fourier-Bessel particle in cell

The FBPIC algorithm was originally developed by Lehe and Kirchen [10] and uses a spectral-cylindrical representation of the field, in contrast to most other PIC algorithms which uses a 3D cartesian grid. The spectral representation means that the fields are transformed into Fourier space, and each coordinate can then be expressed as a Fourier sum and solved for. Afterward, the fields are transformed back to real space. The fields are, in contrast to a differential solver, never staggered in space nor time. This makes the FBPIC relatively computationally fast and accurate for geometries that are close to cylindrical. Since the PIC code, on the other hand, staggers the field in both time and space, some numerical artifacts may occur, one being a numerical growth of the emittance of the relativistic particles. Because of the spectral representation of the field, numerical artifacts that arises from the discretization of fields are avoided [10].

4.4.1 Spectral representation

Spectral Cartesian PIC algorithm solves the Maxwell's equation in Fourier space. A certain class within this class of algorithms, called *Psuedo-Spectral Analytical Time Domain* (PSATD) algorithms, do not suffer from spurious numerical dispersion. It therefore follows that the algorithm is free from associated numerical artifacts. The Maxwell's equations in Eq. (4.2), can in a 3D Cartesian geometry be represented by a sum of Fourier modes as:

$$F_\varphi(\mathbf{r}) = \frac{1}{(2\pi)^3}\int_{-\infty}^{\infty} dk_x \int_{-\infty}^{\infty} dk_y \int_{-\infty}^{\infty} dk_z \mathcal{F}_\varphi(\mathbf{k}) e^{i(k_x x + k_y y + k_z z)}, \tag{4.13}$$

and with the Fourier representation of F as:

$$\mathcal{F}_\varphi(\mathbf{r}) = \int_{-\infty}^{\infty} dx \int_{-\infty}^{\infty} dy \int_{-\infty}^{\infty} dz F_\varphi(\mathbf{k}) e^{-i(k_x x + k_y y + k_z z)}, \tag{4.14}$$

where F is any of the electric and magnetic fields or the current, in any coordinate φ. In this representation, each field may be decoupled and written as, using $\varepsilon_0 = 1/\mu_0 c^2$:

$$
\begin{aligned}
\frac{1}{c^2}\frac{\partial}{\partial t}\mathcal{E}_x &= ik_y\mathcal{B}_z - ik_z\mathcal{B}_y - \mu_0\mathcal{J}_x \qquad & \frac{\partial}{\partial t}\mathcal{B}_x &= -ik_y\mathcal{E}_z + ik_z\mathcal{E}_y \\
\frac{1}{c^2}\frac{\partial}{\partial t}\mathcal{E}_y &= ik_z\mathcal{B}_x - ik_x\mathcal{B}_z - \mu_0\mathcal{J}_y \qquad & \frac{\partial}{\partial t}\mathcal{B}_y &= -ik_z\mathcal{E}_x + ik_x\mathcal{E}_z \\
\frac{1}{c^2}\frac{\partial}{\partial t}\mathcal{E}_z &= ik_x\mathcal{B}_y - ik_y\mathcal{B}_x - \mu_0\mathcal{J}_z \qquad & \frac{\partial}{\partial t}\mathcal{B}_z &= -ik_x\mathcal{E}_y + ik_y\mathcal{E}_x.
\end{aligned} \tag{4.15}
$$

where $\mathcal{E}_i$, $\mathcal{B}_i$, and $\mathcal{J}_i$ are the Fourier counterparts of $\mathbf{E}$, $\mathbf{B}$, and $\mathbf{j}$ respectively. In the form of Eq. (4.15), the fields can be integrated in time, and then transformed back to real space by using Eq. (4.13). The procedure described is the principle of spectral Cartesian algorithms, including PSATD. Now, in cylidrical coordinates, Maxwell's equations becomes:

$$
\begin{aligned}
\frac{1}{c^2}\frac{\partial}{\partial t}E_r &= \frac{1}{r}\frac{\partial}{\partial\theta}B_z - \frac{\partial}{\partial z}B_\theta - \mu_0 j_r \qquad & \frac{\partial}{\partial t}B_r &= -\frac{1}{r}\frac{\partial}{\partial\theta}E_z + \frac{\partial}{\partial z}E_\theta \\
\frac{1}{c^2}\frac{\partial}{\partial t}E_\theta &= \frac{\partial}{\partial z}B_r - \frac{\partial}{\partial r}B_z - \mu_0 j_\theta \qquad & \frac{\partial}{\partial t}B_\theta &= -\frac{\partial}{\partial z}E_r + \frac{\partial}{\partial r}E_z \\
\frac{1}{c^2}\frac{\partial}{\partial t}E_z &= \frac{1}{r}\left(\frac{\partial}{\partial r}rB_\theta - \frac{\partial}{\partial\theta}B_r\right) - \mu_0 j_z \qquad & \frac{\partial}{\partial t}B_z &= \frac{1}{r}\left(-\frac{\partial}{\partial r}rE_\theta + \frac{\partial}{\partial\theta}E_r\right)
\end{aligned} \tag{4.16}
$$

However, in cylindrical coordinates, the representation in Eq. (4.13) is no longer appropriate, since the Fourier modes do not decouple, as they did for the Cartesian coordinates. Instead, the Fourier-Hankel representation may be used [10]:

$$
\begin{aligned}
F_z(\mathbf{r}) =& \frac{1}{(2\pi)^2}\sum_{m=-\infty}^{\infty}\int_{-\infty}^{\infty}dk_z\int_0^\infty k_\perp dk_\perp \hat{\mathcal{F}}_{z,m}(k_z,k_\perp)J_m(k_\perp,r)e^{-im\theta+ik_z z}, \\
F_r(\mathbf{r}) =& \frac{1}{(2\pi)^2}\sum_{m=-\infty}^{\infty}\int_{-\infty}^{\infty}dk_z\int_0^\infty k_\perp dk_\perp (\hat{\mathcal{F}}_{+,m}(k_z,k_\perp)J_{m+1}(k_\perp r) \\
&+ \hat{\mathcal{F}}_{-,m}(k_z,k_\perp)J_{m-1}(k_\perp r))e^{-im\theta+ik_z z}, \\
F_\theta(\mathbf{r}) =& \frac{1}{(2\pi)^2}\sum_{m=-\infty}^{\infty}\int_{-\infty}^{\infty}dk_z\int_0^\infty k_\perp dk_\perp i(\hat{\mathcal{F}}_{+,m}(k_z,k_\perp)J_{m+1}(k_\perp r) \\
&- \hat{\mathcal{F}}_{-,m}(k_z,k_\perp)J_{m-1}(k_\perp r))e^{-im\theta+ik_z z},
\end{aligned} \tag{4.17}
$$

where F has the same representation as before, and J_m denotes the Bessel function of order m and $k_\perp$ comes from the change of variables of k_x and k_y as $k_x = k_\perp\cos(\phi)$ and $k_y = k_\perp\sin(\phi)$. The spectral representation of Eq. (4.17) may now be written as:

$$\hat{\mathcal{F}}_{z,m}(k_z,k_\perp) = \int_{-\infty}^{\infty} dz \int_0^{\infty} rdr \int_0^{2\pi} d\theta F_z(\mathbf{r}) J_m(k_\perp r) e^{im\theta - ik_z z},$$
$$\hat{\mathcal{F}}_{+,m}(k_z,k_\perp) = \int_{-\infty}^{\infty} dz \int_0^{\infty} rdr \int_0^{2\pi} d\theta \frac{F_r(\mathbf{r}) - iF_\theta(\mathbf{r})}{2} J_{m+1}(k_\perp r) e^{im\theta - ik_z z}, \quad (4.18)$$
$$\hat{\mathcal{F}}_{-,m}(k_z,k_\perp) = \int_{-\infty}^{\infty} dz \int_0^{\infty} rdr \int_0^{2\pi} d\theta \frac{F_r(\mathbf{r}) + iF_\theta(\mathbf{r})}{2} J_{m-1}(k_\perp r) e^{im\theta - ik_z z},$$

where $\hat{\mathcal{F}}_- = (\hat{\mathcal{F}}_{x,m-1} + i\hat{\mathcal{F}}_{y,m-1})/2$ and $\hat{\mathcal{F}}_+ = (\hat{\mathcal{F}}_{x,m+1} - i\hat{\mathcal{F}}_{y,m+1})/2$. The z-component, does not transform in the same manner as the r- and θ-component. This is due to the different behaviors of the coordinates close to the axis. Also, scalar fields, such as ρ, transforms in the same manner as F_z. By applying Eq. (4.17) to the spectral representation of the Maxwell's equations, the different modes do indeed decouple. From Eq. (4.18), it can be seen that m represents different azimuthal modes of the form $e^{-im\theta}$. Hence, for physical systems with close to cylindrical symmetry, the Fourier sum in Eq. (4.17) is truncated to a few terms since higher order modes goes to zero when $|m|$ becomes large. Also, from Eq. (4.18), it can be seen that the field now is represented by a set of 2D arrays, $\hat{\mathcal{F}}(k_z, k_\perp)$ instead of a set of 3D arrays $\mathcal{F}(k_x, k_y, k_z)$. In fact, only one 2D grid per azimuthal mode m is used. This reduction leads to a computationally more efficient manipulation of the fields, and it is the representation that the FBPIC algorithm uses to solve the Maxwell's equations in cylindrical coordinates, Eq. (4.16). However, since the number of 2D grids are defined by the number of modes used, one have to make sure that enough modes are used in the simulation to represent the physics. For an ideal LWFA, two modes are enough, where $m = 0$ represents the grid independent of θ, which would be the wakefield in an ideal LWFA. $m = 1$ then represents the the field that varies proportionally with $\cos(\theta)$ and $\sin(\theta)$, which corresponds to a linearly polarized laser field expressed in cylindrical coordinates, E_θ and E_r, given that the propagation is in the z-direction. Higher order modes takes into account the fields that departures from the cylindrical symmetry, and represents fields that varies with $\cos(m\theta)$ and $\sin(m\theta)$. For nonlinear effects, such that self-injection, sometimes 3 modes or more are necessary. However, the computational cost increases with the number of modes used. Therefore, the FBPIC algorithm is not efficient for geometries that are far from cylindrical [10].

In the FBPIC code, the field gathering and current deposition of the macroparticle is not directly performed in spectral space. This is because the operation in spectral space becomes inefficient, since it still just affects a few cells close to the macroparticle in real space, as visualized in Fig. 4.2, making it a local property. While in spectral space, the field is represented on the whole grid, making the operation a global property. Therefore, for the spectral solver, an intermediate grid is used where the field gathering and current deposition can take place. The transformation from the intermediate grid to the spectral grid is then a combination of a Fourier transform along z and Hankel transformation along r. The two transformations lead to different computational costs in each direction due to the different discretizations of the intermediate grid, and therefore limits the number of possible grid points

in each direction. In the z direction, the discretization is commonly done by fast Fourier transform, while the discretization of the Hankel function varies depending on the application [10]. For the FBPIC algorithm, the discretization along r is done by an evenly spaced grid for the intermediate grid. These discretizations leads to the computational cost in of the Fourier transform scales as $N_z \log(N_z)$, since the discretization is done by fast Fourier transform, while the Hankel transform scales as N_r^2, where N_z and N_r are, respectively, the number of grid points along z and r. For a large number of grid points along r, the Hankel transform may therefore dominate the computational cost [10].

4.4.2 Advantages over finite-difference solvers

Other than the already mentioned benefits of using FBPIC in comparison to standard PIC codes which uses a finite-difference solver and full 3D Cartesian grid are for one the accuracy of a spectral solver. Because of their high accuracy numerical artifacts that are present in a finite-difference algorithm are avoided. One of them being spurious numerical dispersion which affect the simulated dephasing length of the LWFA. This is not present at all in a spectral solver. For a typical finite-difference solver, the force felt by an electron co-propagating in a laser is over estimated, which mainly is a consequence of the discretization of the $\mathbf{E}$ and $\mathbf{B}$ fields. The discretization in turn leads to an improper compensation of the fields in Lorentz equation, $\mathbf{F} = -e(\mathbf{E} + \mathbf{v} \times \mathbf{B})$. However, since the fields in the FBPIC algorithm are not discretized, the calculated force on an electron from the field is thus correct [10].

Even though the spectral quasi-cylindrical representation utilized in FBPIC is advantageous, it does not come without shortcomings. One of them being that a spectral algorithm is normally more difficult to parallelize. Another is that the implementation of boundary condition for the moving window is normally more complicated for a spectral algorithm. Nevertheless, the accuracy of spectral solvers can, depending on their application, still be preferred over finite-difference solvers [10].

4.5 Simulation parameters

In the FBPIC input-file, the simulation box, and resolution must be specified. Other than that, the density profile must be given, and this could for example be the density modulation that was presented in section 3.5. For this project, the density modulation that is described by Eq. (3.17) is in particular studied, since it was proposed in [2] as a step towards the generation of attosecond electron pulses, which this project is dedicated to.

An example of an input-file that calls the FBPIC simulation is shown in appendix A.2. Other than the already mentioned parameters, the normalized vector potential, a_0, background electron density of the plasma, n_e, duration, τ_0, and beam waist, w_0, of the laser must be specified. The a_0, w_0 and n_e are obtained by using the

matching conditions in table 3.1 based on the new laser system in table 1.1. Thus, the so called matched parameters can be seen in table 4.1.

Table 4.1: *Matched parameters, derived from the new laser parameters specified in table 1.1.*

Parameter	Quantity
a_0	3.4
w_0	3.1 [µm]
n_e	$4{\cdot}10^{19}$ [cm^{-3}]

From the matched parameters, a dephasing length of $L_d = 90$ µm and an energy gain of $\Delta W = 50$ MeV can be expected.

4.5.1 The density profile

The density profile used in the simulations can be seen in Fig. 4.4, where α is the amplitude of the density modulation, measured from the plateau to the maximum of the "hill". The α is swept over values from $\alpha = 0$ to $\alpha = 0.6$ for most of the simulations. In the figure, the dashed black line marks the focal plane of the laser. Over the plateau, the density is kept at the background number density, n_e.

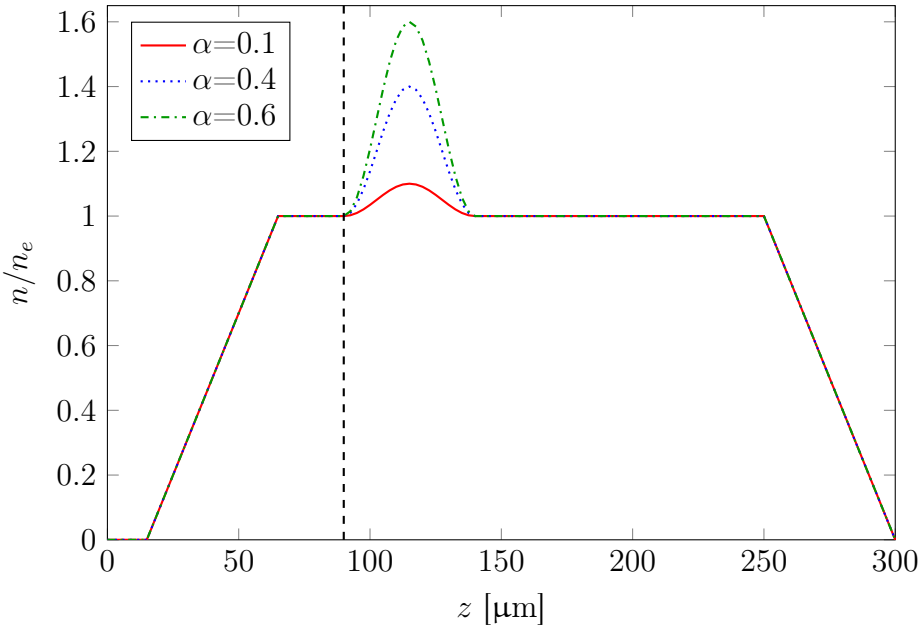

Fig. 4.4: *The density profile used in the simulations, described mathematically by Eq.* (3.17)*. α is varied in the simulations.*

An $\alpha = 0$ would in this case correspond to a flat density profile, i.e. no density modulation. For the simulation performed with this scheme, the focal plane is positioned at the beginning of the plateau.

4.5.2 Laser specification

The excitation of the wakefield is dependent on the laser profile used for the simulation. For the simulation of this project, a few-cycle laser profile has been used, due to the short duration of the laser pulse. In the FBPIC code, the electric field profile for such a laser is given by [10, 30]:

$$E(\mathbf{x},t) = \Re\left[a_0 E_0 \exp(i\phi_{cep})\frac{iZ_R}{q(z)}\left(1+\frac{ik_0}{s}\left(z-z_0-ct+\frac{r^2}{2q(z)}\right)\right)^{-(s+1)}\right]. \quad (4.19)$$

In this context, r gives the transverse direction of the laser propagation, and $\mathbf{x}$ represents the spatial coordinates. E_0 corresponds to the electric field amplitude for $a_0 = 1$, $q(z) = z - z_f - iZ_R$, ϕ_{cep} is the carrier-envelope phase, and s is a parameter that controls the pulse duration [30]:

$$\omega_0\tau_0 = s\sqrt{2(4^{1/(s+1)}-1)}. \quad (4.20)$$

As $\omega_0\tau_0 \gg 1$, the few-cycle laser profile in Eq. (4.19) approaches that of a Gaussian pulse. The few-cycle laser profile is used during this project because as the initialized laser pulse becomes short, the standard Gaussian laser pulse is not well adapted in the FBPIC code. This is because the defined Gaussian laser pulse profile of the algorithm does not take into account that different frequencies focus in different ways. It has been seen in initial tests of this project that there is a significant difference between the Gaussian pulse and few cycle laser profile for a FWHM duration of τ_0= 7 fs.

The laser is by default linearly polarized in the x-direction, given that the laser propagates in the z-direction of a Cartesian coordinate system. In the simulation box, the laser is initialized directly on the grid, leading to the fields satisfying the equations $\nabla \cdot \mathbf{E} = 0$ and $\nabla \cdot \mathbf{B} = 0$.

5

Results and discussion

The matched parameters given in section 4.5 are used as a reference for each of the simulations performed in this project. In particular, the matched n_e caused some numerical instabilities in the simulations. Also, two injection mechanisms are present, as will be shown in section 5.3. Therefore, n_e was decreased, and the results from this are shown in section 5.1 and 5.2.

5.1 Density modulation

To suppress self-injection, the number density of the background plasma was decreased until no injection was observed for a flat density profile, corresponding to $\alpha = 0$ in Fig. 4.4. This happened when $n_e = 1 \cdot 10^{19}$ cm^{-3}, i.e. at n_e four times less the matched density in table 4.1. For this number density, w_0 was too small, and the self-focusing effect was unable to cancel out the spatial diffraction.

The problem was solved by increasing w_0 in the simulation, while maintaining the same a_0, which corresponds to a laser pulse energy four times greater than that specified in table 1.1. So, the parameters given in the input-file are thus $a_0 = 3.4$, $w_0 = 6.2$ µm and lastly, $n_e = 1 \cdot 10^{19}$ cm^{-3}. A snapshot from three instances of the simulation performed for $\alpha = 0.4$ can be seen in Fig. 5.1. In the figure, (a) and (b) are the charge density and the longitudinal phase space (z, u_z) before the density modulation in Fig. 4.4, and just at the focal plane of the laser. The bubble is almost spherical, and as can be seen in phase space, no electrons are present within the bubble. Hence, self-injection is suppressed, as expected. The injection occurs at a position about half-way through the down-ramp region of the modulated density. Fig. 5.1(c)-(d) shows the charge density and phase space right after the density modulation. In the longitudinal phase space, it can be seen that at this point there is only one electron pulse present. In Fig. 5.1(e)-(d) the charge density and longitudinal phase space are lastly shown at a position right before the end of the plateau in Fig. 4.4. The injected electron pulse has at this point almost been accelerated over a distance of 100 µm. In phase space at this point, a U-shape can be observed, which indicates that the particle energy distribution is peaked, with the majority of the particles having a normalized momentum of $u_z = 80 m_e c$, which in turn corresponds to a peak particle energy of approximately 40 MeV.

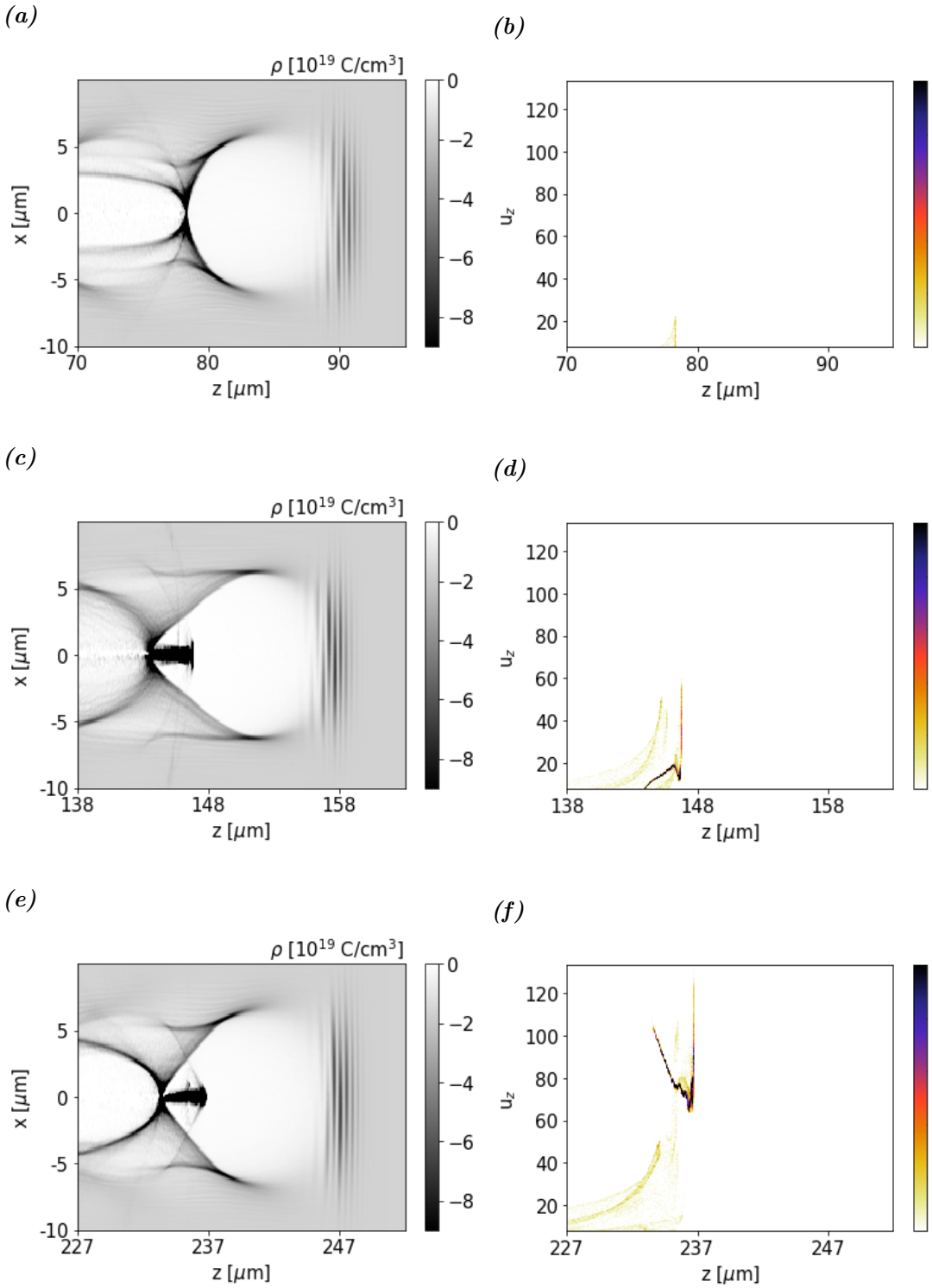

Fig. 5.1: *Snapshots of the charge density and corresponding longitudinal phase space at three instances of time for the parameters a_0=3.4, n_e=1·10^{19} cm^{-3}, w_0=6.2 μm and α=0.4. In (a) and (b), right before the density modulation, (c) and (d), right after and (e) and (f), right before the end of the plateau in Fig. 4.4.*

In Fig. 5.2, the charge density, the accelerating electric field, and the electric field of

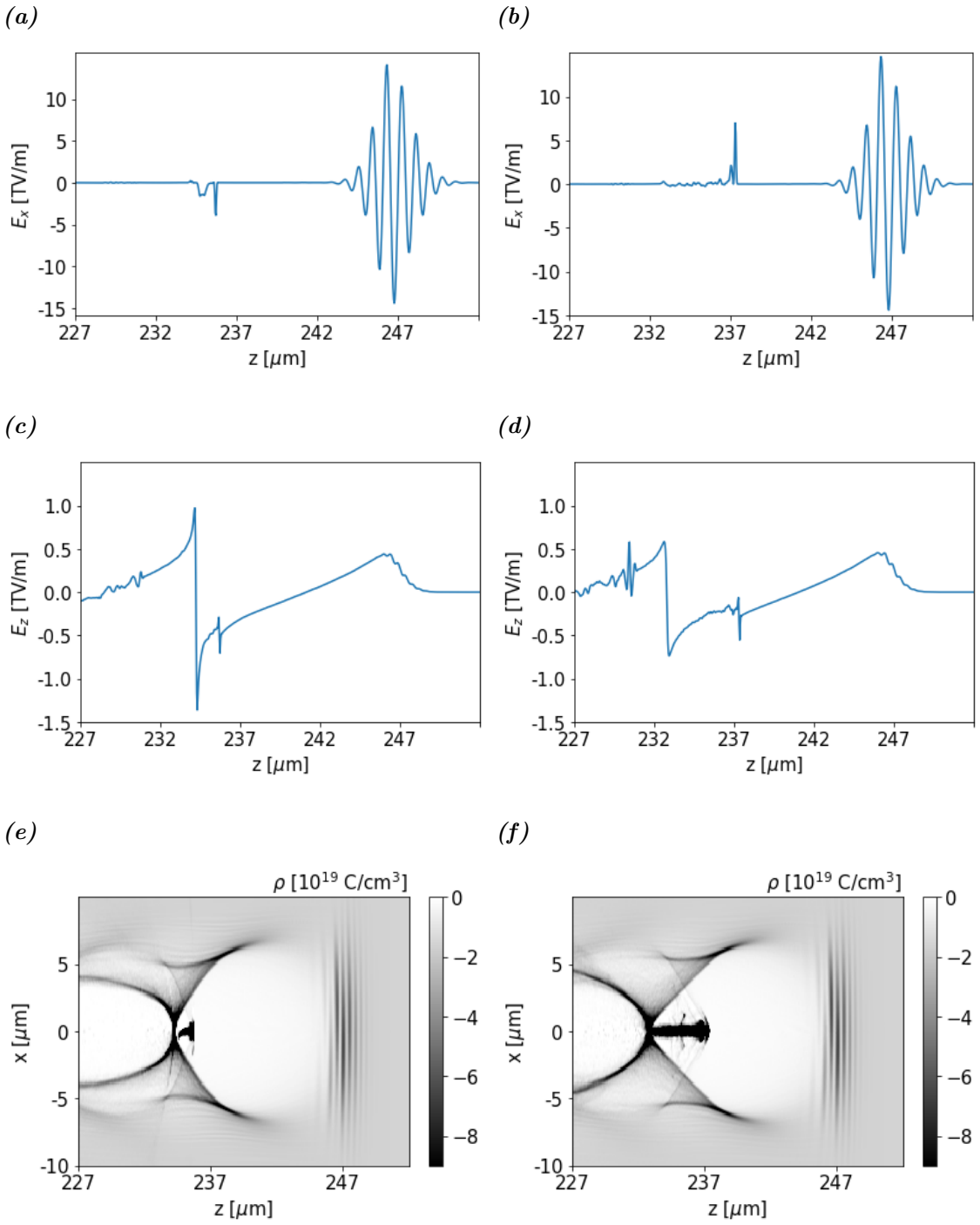

Fig. 5.2: *Snapshots of the laser's electric field, electric field along the bubble, and charge density from simulations performed for the parameters* a_0*=3.4,* n_e*=1·10*^{19} *cm*$^{-3}$*, and* w_0*=6.2 µm. In (a), (c), and (e)* α*=0.1. In (b), (d), and (f) alpha=0.6.*

the laser are shown at an instance right before the end of the plateau in Fig. 4.4. In Fig. 5.2(a), (c), and (e), $\alpha = 0.1$, while in Fig. 5.2(b), (d), and (f) $\alpha = 0.6$. As can be seen, there is a minor difference in the strength of the electric field of the laser, where it is greater for $\alpha = 0.6$. This might be because the higher α causes a greater self-focusing effect. It could, however, also be some numerical artifacts that causes the difference, but this has not been studied in more detail during this project.

However, for $\alpha = 0.6$, more electrons are injected into the bubble, in comparison to when $\alpha = 0.1$. The amount injected electrons are such that they significantly affect the accelerating field, E_z, by decreasing the field's gradient. It is thus expected that an increased α leads to an increased charge injection, hence a lower particle energy. This is exactly what can be observed in Fig. 5.5(b). However, as shown in Eq. (3.16), the spatial length of the electron bunch, scales with Q^2. Moreover, as the number of injected electrons increases, so does the duration of the electron pulse. This can be seen in Fig. 5.3 for α =0.2, 0.4, and 0.6. Indeed, the FWHM duration, τ_e, do increase slightly with increasing α. The energy spectrum for the same simulations as in Fig. 5.3 can be seen in Fig. 5.4.

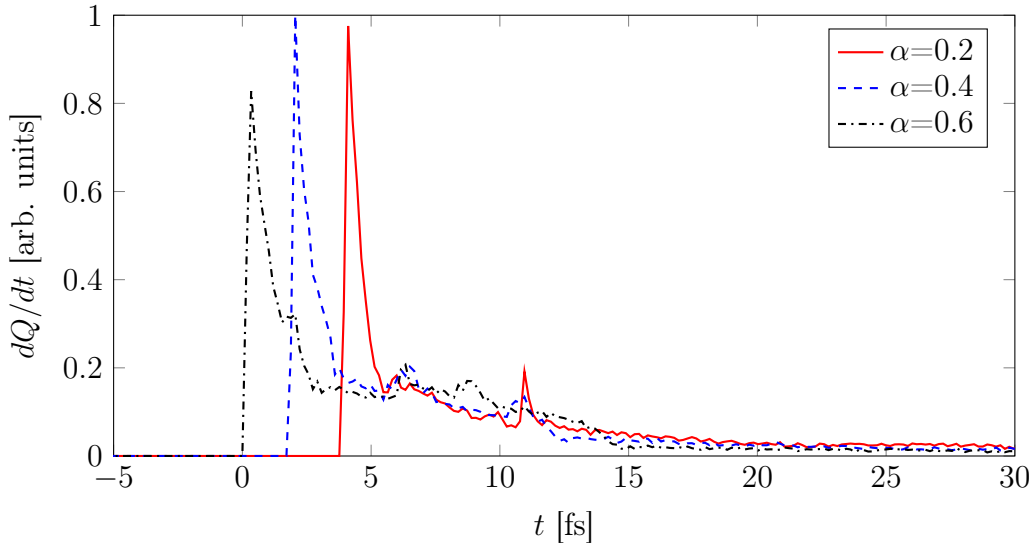

Fig. 5.3: *The temporal profile of 3 electron pulses from the simulations where* a_0*=3.4,* w_0*=6.2 μm and* n_e*=1·10*^{19} *cm*$^{-3}$.

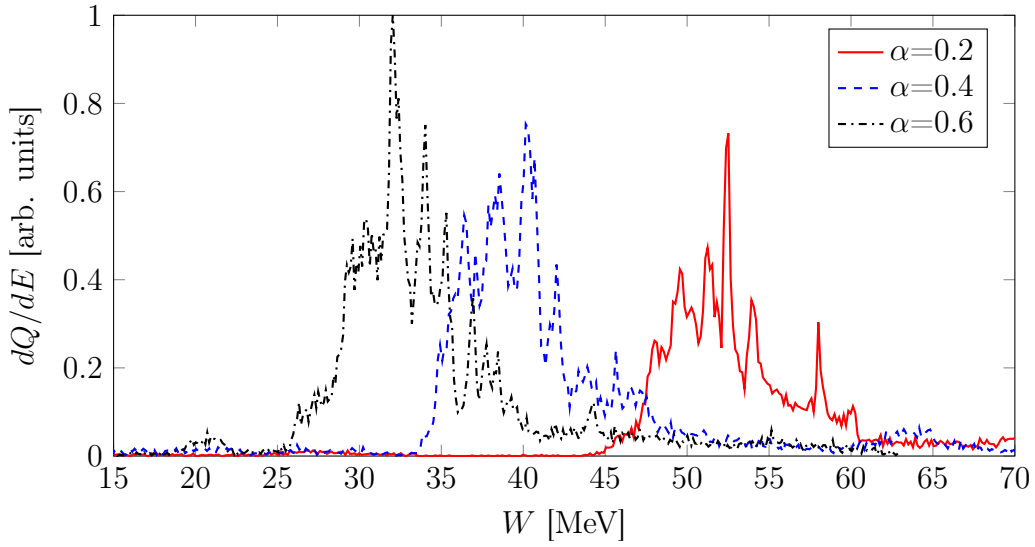

Fig. 5.4: *The energy spectrum of 3 electron pulses from the simulations where* a_0*=3.4,* w_0*=6.2 μm and* n_e*=1·10*^{19} *cm*$^{-3}$.

The FWHM duration and current for all α which were simulated in this project can be seen in Fig. 5.5(a). This again shows that duration of the electron pulse increases with increasing α because more electrons are injected in the process. Another result is that attosecond electron pulses can be generated by utilizing the density profile presented in Fig. 4.4, if the laser pulse energy is four times greater than the energy specified for the new laser system in table 1.1. Fig. 5.5(b) shows the particle energy and spread for the same simulations as in Fig. 5.5(a). It can be observed that for the simulations performed here, the highest particle energy is obtained for $\alpha = 0.1$, as expected, which corresponds to the electron pulse with the least amount of charge. However, at $\alpha = 0.1$ the energy spread is larger than it is for e.g. $\alpha = 0.15$ up to $\alpha = 0.3$. This might be because of some numerical error, since it does not follow the general trend that can be seen in Fig. 5.5(b). However, it might be that for $\alpha < 0.1$, the energy spread increases. The reasons why is that the effect of beam-loading is not as significant for small a small α. Also, for a smaller α the electrons are located further back in the bubble, and hence experience a stronger **E**-field. To fully establish if it is an artifact or physics, simulations for some α's below 0.1 must be performed.

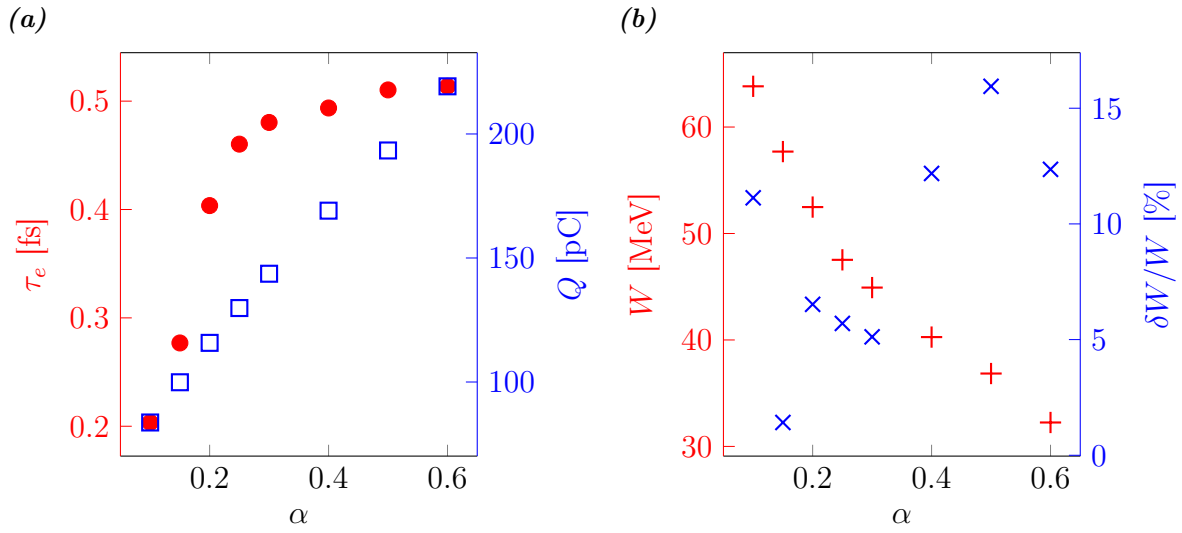

Fig. 5.5: *In (a) the FWHM duration, τ_e, of the electron pulses and their charge, Q, for each α simulated in this project. (b), their respective particle energy and energy spread.*

In Fig. 5.5(b) it can also be seen that the highest energy gain is approximately 64 MeV, which is higher than the expected energy gain described in section 4.5, where it was expected that $\Delta W = 50$ MeV. This is not surprising, because as the number density decreases, the energy gain will increase, as seen in Eq. (3.14). However, the energy gain does also depend on the acceleration length, and as can be seen in Eq. (3.10), the dephasing length increases with decreasing n_e. Therefore, if $L_{acc} \approx L_d$, then ΔW again increases. The electrons could probably be accelerated over a longer distance than done here in these simulations. In that case, even higher particle energies would be obtainable, assuming that the acceleration stops before dephasing occur.

5.1.1 Decreasing a_0

The results so far show that the generation of attosecond electron pulses benefit from a laser pulse waist twice as large as the matched beam waist, which corresponds to a laser pulse with four times higher energy than the one specified in table 1.1. At least if n_e is decreased such that self-injection is suppressed. A simulation with decreased intensity, corresponding to $a_0 = 1.7$ was performed to see if a lower intensity still could excite a nonlinear plasma wave. In this case, the plasma wave is weakly relativistic, which can be seen in Fig. 5.6. Also, no injection occur in the first plasma period, even though density modulation is utilized, with $\alpha = 0.4$. In this case, the phase velocity of the back of the bubble is not slowed down enough for the electrons to be injected. However, in the second and even third plasma period, electrons are injected. This is because the relative change in the bubble phase velocity increases with increasing plasma period. Injection is therefore more likely to happen as the plasma period increases.

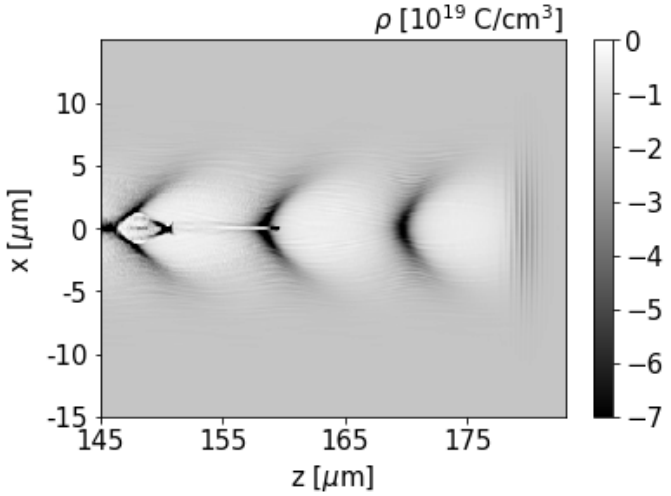

Fig. 5.6: *A snapshot of a simulation performed for the parameters n_e=1·10^{19}, a_0=1.7, w_0=6.2 μm and α=0.4.*

5.2 The effect of the beam waist

For the simulations performed, $n_e = 1 \cdot 10^{19}$ cm^{-3}. In this case, none of the parameters are matched. The sole purpose was to suppress self-injection, such that the only injection mechanism is due to the density modulation. Therefore, a_0 and w_0 are the matched parameters, as presented in table 4.1. It was interesting here to see if there were any significant difference between the simulations performed for $w_0 = 6.2$ μm and $w_0 = 3.1$ μm. These comparisons were done by investigating the evolution of a_0 as the laser propagates through the plasma density. The result can be seen in Fig. 5.7.

As can be seen in Fig. 5.7, the evolution of a_0 as the laser propagates through is significantly different in the both cases. In Fig. 3.3(b), the self-focusing effect of the plasma is unable to effectively cancel the spatial diffraction of the laser pulse, hence

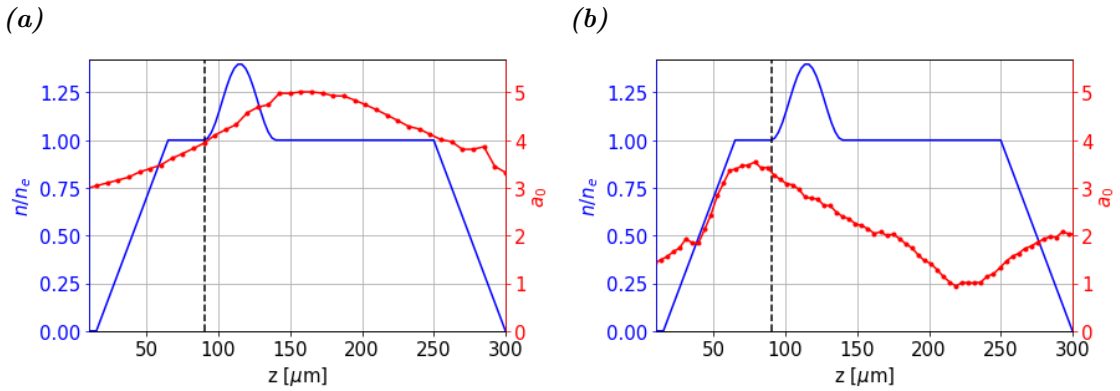

Fig. 5.7: *The evolution of a_0 for simulations with parameters a_0=3.4, μm, n_e=1·10^{19} cm^{-3}, and (a) w_0=6.2 μm and (b) w_0=3.1 μm.*

the decrease in a_0.

The charge density and the longitudinal phase space from the density down-ramp injection, similar to the density profile shown in Fig. 5.7(b) can be seen in Fig. 5.8. In comparison to the longitudinal phase space in Fig. 5.1, the particle distribution does not form into a U-shape, but rather has a continuous streak. This means that the energy distribution is broad, and not as peaked as it is for the simulations performed with a $w_0 = 6.2$ μm.

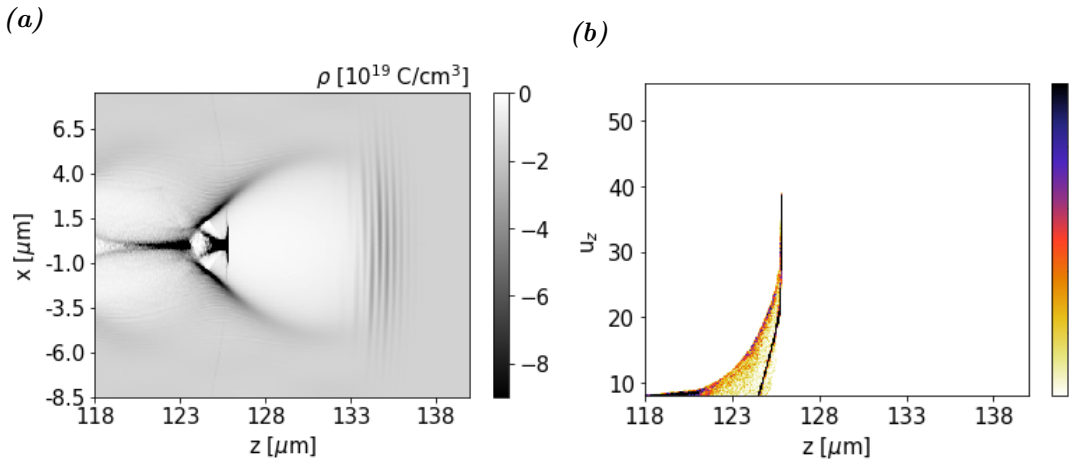

Fig. 5.8: *A snapshot from the simulation where a_0=3.4, w_0=3.1 μm, n_e=1·10^{19} cm^{-3}. In (a), the charge density and in (b) the corresponding longitudinal phase space.*

5.3 Numerical instabilities at a high n_e

When the matched parameters defined in table 4.1 are given as an input to the simulation, numerical instabilities occur. This might have arisen because of the increased number density in comparison to the other simulations, and therefore the given resolution was not enough to resolve the actual physics. One problem, however, with

performing LWFA for a high number density together with a density modulation is the fact that two injection mechanisms might occur, which is shown in Fig. 5.9. One electron pulse is firstly injected before the density modulation, and the second is injected at the down-ramp. It this point, because of the resolution related instabilities, it is unclear whether the two injection occur because of the underlying physics, or if it is due to the instability at the current resolution.

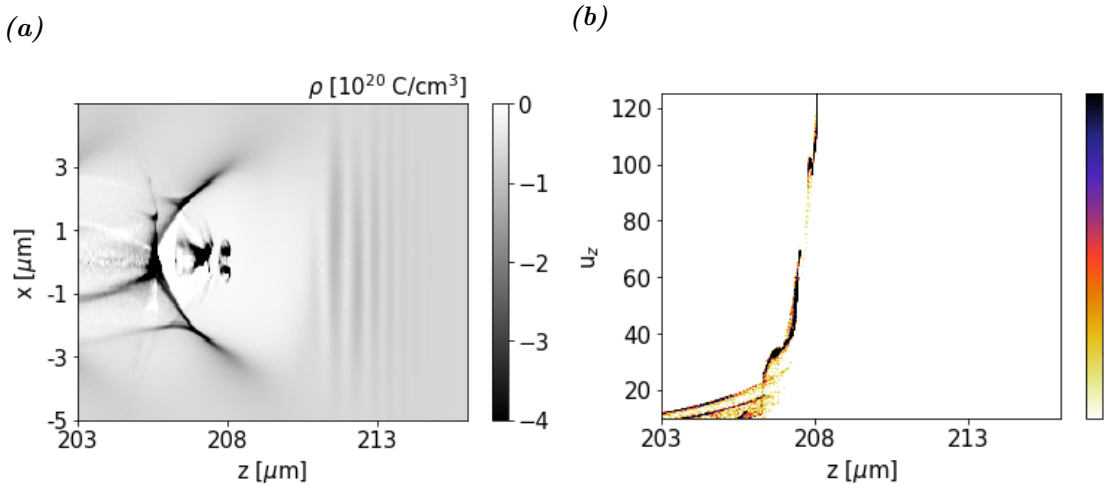

Fig. 5.9: *A snapshot from the simulation where the number density was $n_e = 4 \cdot 10^{-19}$ cm^{-3}, $a_0 = 3.4$ and $w_0 = 3.1$ μm. In (a), the charge density can be seen, and in (b) the corresponding longitudinal phase space.*

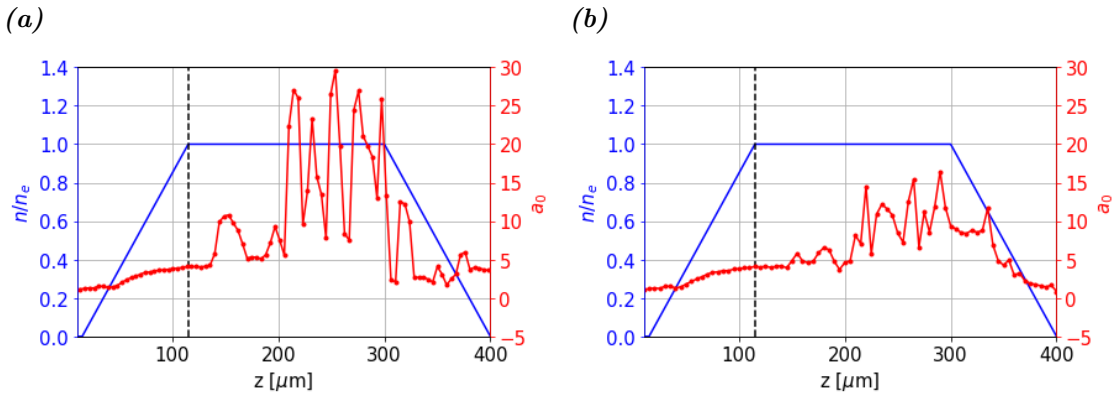

Fig. 5.10: *The evolution of a_0 over a flat density profile for two different number of azimuthal modes, m. In (a) $m = 2$, and in (b) $m = 4$.*

It did turn out however, that the instabilities were severe, and it could be that either the resolution was too low to resolve the physics. However, for these simulations, the parameter limiting the possible resolution was the VRAM of the graphics card used, with the specifications seen in appendix B.1. Another possibility was that the number of azimuthal modes used for the simulations, i.e. $m = 2$, was not enough to capture eventual asymmetries. Therefore, a test with a flat density profile, was performed for $m = 2, 3, 4$ modes. In Fig. 5.10, the evolution of a_0 can be seen, for the simulation results from $m = 2$ and $m = 4$. The oscillations of a_0 occurs in both cases, and it indicates that more modes might be needed, hence, the problem might

not be nearly cylindrical.

The resolution was checked by decreasing the simulation box's size to about 2/5 of the previous one, while keeping the number of gridpoints as specified in table A.1. For this simulation, even though the number of azimuthal modes at this point was $m = 4$, numerical instabilities occurs at an early stage of the simulation. It could be that the simulation box was made too small, and cut the electric field off. Another simulation was performed to check this, where the simulation box was slightly larger. The same effect was not observed. It is deduced that not only must the resolution and the number of modes used be enough to resolve the physics, but the simulation box must be made large enough to capture the full interaction.

6

Conclusion and outlook

The simulations results show that by tailoring the number density of the plasma, it is possible to obtain sub-fs electron pulses from the LWFA, and by matching the laser waist to the plateau density, in particular, by choosing laser parameters corresponding to an energy four times larger than the laser system that the division of Atomic physics plans to purchase during 2020. The resulting particle energy of the electron pulses was peaked with a small energy spread. Another important parameter for an accelerator is the emittance, but it was not investigated because it requires high resolution simulation. The sub-fs duration of the electron pulses simulated here are promising, as this shows that ultrashort electron pulses may be achievable with the new laser system. These short pulse duration were achieved with a small density modulation, and the shortest electron pulse also had the highest particle energy. However, the small density modulation led to the smallest amount of injected electrons, and in terms of injected charge and energy, there seems to be a trade-off in how to choose these two parameters. In future works, it would be interesting to investigate the evolution of the electron pulse, such as the divergence, after it leaves the plasma and propagates some distance afterwards.

Throughout this project, the simulations has been carried out on a local computer server. In the future, simulation on a cluster would be preferable, since it offers greater resolution and sweeping of parameters made easier through parallelization. Nevertheless, using a local computer for a fast diagnosis has been advantageous for this project, and will most likely be for similar projects in the future, given that the computer is equipped with a GPU with greater VRAM. Also, larger simulations, where the computations are made in the boosted Lorentz-frame would be interesting to perform. Instead of the simulation frame moving in the reference frame, it is moving in the Lorentz-frame together with the laser. As a consequence, the plasma is shorter and moves towards the laser pulse. In this regime the algorithm is stable and performs iterations faster than in the lab-frame, which becomes more relevant with larger simulations.

References

[1] S. Thorin, J. Andersson, F. Curbis, M. Eriksson, O. Karlberg, D. Kumbaro, E. Mansten, D. Olsson, and S. Werin. The MAX IV linac. In *27th International Linear Accelerator Conference*, number LINAC-2014-TUIOA03, pages 400–403, Geneva, Switzerland, 2014.

[2] M. P. Tooley, B. Ersfeld, R. Yoffe, A. Noble, E.Brunetti, Z. M. Sheng, M. R. Islam, and D. A. Jaroszynski. Towards attosecond high-energy electron bunches: Conrtrolling self-injection in laser-wakefield accelerators through plasma-density modulation. *Physical Review Letters*, 119(4):044801, July 2017.

[3] E. Esarey, C. B. Schroeder, and W. P. Leemans. Physics of laser-driven plasma-based electron accelerators. *Reviews of modern physics*, 81(3):1229–1285, Aug. 2009.

[4] T. Tajima and J. M. Dawson. Laser electron accelerator. *Physical review letters*, 43(4), Jul. 1979.

[5] S. Bulanov, N. Naumnova, F. Pegoraro, and J. Sakai. Particle injection into the wave acceleration phase due to nonlinear wake wave breaking. *Physical Review E*, 58(5), Nov. 1998.

[6] M. Hansson, B. Aurand, X. Davoine, H. Ekerfelt, K. Svensson, A. Persson, C.-G. Wahlström, and O. Lundh. Down-ramp injection and independently controlled acceleration of electrons in a tailored laser wakefield accelerator. *Physical review letters special topics - accelerators and beams*, 18(7):071303, 2015.

[7] H. Ekerfelt, M. Hansson, I. Gallardo González, X. Davoine, and O. Lundh. A tunable electron beam source using trapping of electrons in a density down-ramp in laser wakefield acceleration. *Scientific reports*, 7(12229), 2017.

[8] J. M. Dawson. Particle simulation of plasmas. *Reviews of modern physics*, 55(2):403–447, 1983.

[9] C. K. Birdsall. Particle-in-cell charged-particle simulations, plus monte carlo collision with neutral atoms, PIC-MCC. *IEEE transactions on plasma science*, 19(2):65–85, April 1991.

[10] R. Lehe, M. Kirchen, I. A. Andiyasch, B. B. Godfreyad, and J.-L. Vaya. A spectral, quasi-cylindrical and dispersion-free particle-in-cell algortihm. *Computer physics communications*, 203:66–82, June 2016.

[11] S. M. Hooker. Development in laser-driven plasma accelerators. *Nature photonics*, 7, Sep. 2013.

[12] Bahaa E. A. Saleh and Malvin Carl Teich. *Fundamentals of photonics*. Wiley Sons, second reprint edition, 2014. ISBN: 978-81-265-3774-7.

[13] Günther Lehner. *Electromagnetic field theory for Engineers and Physicists*, chapter 1. Springer-Verlag Berlin Heidelberg, 2010.

[14] B. Cros. Laser-driven plasma wakefield: propagation effects. `https://doi.org/10.5170/CERN-2016-001.207`, Nov. 2014. Edited by B. Holzer, 2016. Accessed 11/06/2020.

[15] Isabel Gallardo González. *Development and applications of a laser-wakefield x-ray source*. PhD thesis, Department of Physics, Faculty of Engineering, Lund University, 2018.

[16] W. Lu, M. Tzoufras, C. Joshi, F.S. Tsung, W. B. Mori, J. Vieira, R. A. Fonseca, and L. O. Silva. Generating multi-GeV electron bunches using single stage laser wakefield acceleration in a 3D nonlinear regime. *Physical Review Special Topics - Accelerators and Beams*, 10(6), 2007.

[17] W. B. Mori. The physics of the nonlinear optics of plasmas at relativistic intensities for short-pulse lasers. *IEEE Journal of Quantum electronics*, 33(11), Nov. 1997.

[18] V. Malka. Laser plasma accelerators. In P. McKenna, D. Neely, R. Bingham, and D. Jaroszynzki, editors, *Laser-Plasma Interactions and Applications*, Scottish Graduate Series, chapter 11. Springer, Heidelberg, 2013.

[19] Donna Strickland and Gerard Mourou. Compression of amplified chirped optical pulses. *Optical Communications*, 53(3), 1985.

[20] A. Modena, Z. Najmudin, A. E. Dangor, C. E. Clayton, K. A. Marsh, C. Joshi, V. Malka, C. B. Darrow C. Danson, D. Neely, and F. N. Walsh. Electron acceleration from the breaking of relativistic plasma waves. *Nature*, 377:606 – 608, 1995.

[21] C. G. R. Geddes, Cs. Toth, J. van Tilborg, E. Esarey, C. B. Schroeder, D. Bruhwiler, C. Nieter, J. Cary, and W. P. Leemans. High-quality electron beams from a laser wakefield accelerator using plasma-channel guiding. *Nature*, 431:538–541, 2004.

[22] S. P. D. Mangles, C. D. Murphy, Z. Najmudin, A. G. R. Thomas, J. L. Collier, A. E. Dangor, E. J. Divall, P. S. Foster, J. G. Gallacher, C. J. Hooker amd D. A. Jaroszynski, A. J. Langley, W. B. Mori, P. A. Norrey, F. S. Tsung, R. Viskup, B. R. Walton, and K. Krushelnick. Monoenergetic beams of relativistic electrons from intense laser-plasma interactions. *Nature*, 431:535 – 538, 2004.

[23] J. Faure, Y. Glinec, P. Pukhov, S. Kiselev, S. Gordienko, E. Lefebvre amd J.-P-Rousseau amd F. Burgy, and V. Malka. A laser-plasma accelerator producing monoenergetic electron beams. *Nature*, 431:541–544, 2004.

[24] Karl Schmid. *Laser wakefield electron acceleration*. Springer-Verlag Berlin Heidelberg, 2011.

[25] A. Pukhov and J. Meyer-Ter-Vehn. Laser wakefield acceleration: the highly non-linear broken-wave regime. *Applied Physics B*, (74):355–361, 2002.

[26] H. Suk, N. Barov, J. B. Rosenzweig, and E. Esarey. Plasma electron trapping and acceleration in a plasma wake field using a density transition. *Physical review letters*, 86(6), Feb. 2001.

[27] A.J. Gonsalves, K. Nakamura, C. Lin, D. Panasenko, S. Shiraishi, T. Sokollik, C. Benedetti, C. B. Schroeder, C. G. R. Geddes, J. van Tilborg, J. Osterhoff, E. Esarey, C. Toth, and W. P. Leemans. Tunable laser plasma accelerator based onlongitudinal density tailoring. *Nature Physics*, 7:862–866, Aug. 2011.

[28] A. P. L. Robinson. Particle-in-cell and hybrid simulation. In P. McKenna, D. Neely, R. Bingham, and D. Jaroszynzki, editors, *Laser-Plasma Interactions and Applications*, Scottish Graduate Series, chapter 15. Springer, Heidelberg, 2013.

[29] FBPIC contributors. FBPIC algorithm & features, 2016. `https://fbpic.github.io/overview/pic_algorithm.html`. Accessed 20/6/2020.

[30] C. F. R. Caron and R. M. Potvliege. Free-space propagation of ultrashort pulses: Space-time couplings in gaussian pulse beams. *Journal of Modern Optics*, 46(13):1881–1891, 1999.

[31] NVIDIA corporation. CUDA C++ programming guide, June 2020. `https://docs.nvidia.com/cuda/cuda-c-programming-guide/index.html`. Accessed 22/6/2020.

Appendix A

FBPIC input file

A.1 Resolution specifications

In this project, the simulation box was chosen with the current beam waist and laser duration taken into consideration. A rule of thumb when choosing the the simulation box is to set $z_{max} \geq 3c\tau_0$, where τ_0 is the pulse duration of the simulated laser pulse, and $r \geq 3w_0$. This is to ensure that bubble and the laser is not cut off by the simulation box. A compilation of the number gridpoints and macroparticles used can be seen in table A.1. These numbers have not been varied for each and every simulation because of the increase in computaional cost.

Table A.1: *A compilation of the number of gridpoints and macroparticles used during the simulations.*

Number of gridpoints along z	N_z	1600
Number of gridpoints along r	N_r	200
Number of macroparticles along z	M_z	2
Number of macroparticles along r	M_r	2
Number of macroparticles along θ	M_θ	8

One benefit of using the FBPIC code is that all parameters are given in SI-units, except for a_0, which is given in normalized units.

The output from the simulation gives a meta-file for each iteration, containing information about the electric and magnetic field, the current and current density, also the position and momentum of the different species used in the simulation. The macroparticles weight are also obtainable from the meta-files. In this project, the open source python package OpenPMD viewer has been used to analyzing output data from the simulation.

A.2 Example code

Below is an example code, which has been downloaded from the FBPIC web documentation, and slightly modified to suit this project.

```
"""
This is a typical input script that runs a simulation of
laser-wakefield acceleration using FBPIC.

Usage
-----
- Modify the parameters below to suit your needs
- Type "python lwfa_script.py" in a terminal

Help
----
All the structures implemented in FBPIC are internally documented.
Enter "print(fbpic_object.__doc__)" to have access to this
    documentation,
where fbpic_object is any of the objects or function of FBPIC.
"""

# -------
# Imports
# -------
import numpy as np
import math
from scipy.constants import c, e, m_e
# Import the relevant structures in FBPIC
from fbpic.main import Simulation
from fbpic.lpa_utils.laser import add_laser_pulse, FewCycleLaser
from fbpic.openpmd_diag import FieldDiagnostic, ParticleDiagnostic,
    \
     set_periodic_checkpoint, restart_from_checkpoint

# ----------
# Parameters
# ----------

# Whether to use the GPU
use_cuda = True

# Order of the stencil for z derivatives in the Maxwell solver.
# Use -1 for infinite order, i.e. for exact dispersion relation in
# all direction (adviced for single-GPU/single-CPU simulation).
# Use a positive number (and multiple of 2) for a finite-order
    stencil
# (required for multi-GPU/multi-CPU with MPI). A large `n_order`
    leads
# to more overhead in MPI communications, but also to a more
    accurate
# dispersion relation for electromagnetic waves. (Typically,
# `n_order = 32` is a good trade-off.)
# See https://arxiv.org/abs/1611.05712 for more information.
n_order = -1

# The simulation box
Nz = 1600          # Number of gridpoints along z
zmax = 20.e-6     # Right end of the simulation box (meters)
zmin = -40.e-6    # Left end of the simulation box (meters)
Nr = 200           # Number of gridpoints along r
```

```
rmax = 20.e-6    # Length of the box along r (meters)
Nm = 2           # Number of modes used

# The simulation timestep
dr = rmax/Nr
dz = (zmax-zmin)/Nz
dt = dz/c   # Timestep (seconds)

# The particles
p_zmin = 15.e-6  # Position of the beginning of the plasma (meters)
p_zmax = 300.e-6 # Position of the end of the plasma (meters)
p_rmax = 20.e-6  # Maximal radial position of the plasma (meters)
n_e = 1.e19*1.e6 # Density (electrons.meters^-3)
p_nz = 2         # Number of particles per cell along z
p_nr = 2         # Number of particles per cell along r
p_nt = 8         # Number of particles per cell along theta

# The laser
a0 = 3.4          # Laser amplitude
w0 = 6.2*1.e-6       # Laser waist
ctau = 2.1*1.e-6     # Laser duration
tau = ctau/c

z0 = 0.e-6      # Laser centroid -- initial position of the
    centroid in the lab frame
zf = 90.e-6   # Laser focal plane


# The moving window
v_window = c       # Speed of the window

# The diagnostics and the checkpoints/restarts
diag_period = 200         # Period of the diagnostics in number of
    timesteps
save_checkpoints = False # Whether to write checkpoint files
checkpoint_period = 100  # Period for writing the checkpoints
use_restart = False      # Whether to restart from a previous
    checkpoint
track_electrons = False  # Whether to track and write particle ids

# The density profile
zstart = 15.e-6                              # Start position of
    density profile (ramp)
zramp = 50.e-6                               # Ramp length
zw = 25.e-6                                    # Width of density "
    hill"
zi = 100.e-6                                # Position of nozzle,
    central part of the hill
zposstart = -zw + zi                         # The start of the hill
zposend = zw + zi                            # End position of the
    hill
zpos = np.linspace(zposstart,zposend,20)  # The coordinates over
    which the hill is calculated
zplateau = 250.e-6

npeak = 0.6                                    # percental increase
nplateau = 1
nbump = nplateau + npeak*np.cos(math.pi*(zpos-zi)/(2*zw))**2  #
```

```
    Calculating the coordinates of the hill

104
def dens_func( z, r ) :
106     """Returns relative density at position z and r"""
     zp = np.concatenate([np.array([0, zstart, zstart+zramp]),
    zstart+zpos,
108         np.array([zplateau, zplateau+zramp])])
     fp = np.concatenate([np.array([0, 0, nplateau]), nbump, np.
    array([nplateau, 0])])
110     n = np.interp(z,zp,fp,0,0)
     return(n)
112
# Interaction time (seconds) (to calculate number of PIC iterations
    )
114 T_interact = ((zplateau+zramp)+2*(zramp+zmax-zmin))/ v_window


116
# ----------------------------
118 # Carrying out the simulation
# ----------------------------
120
# NB: The code below is only executed when running the script,
122 # (`python lwfa_script.py`), but not when importing it (`import
    lwfa_script`).
if __name__ == '__main__':
124
     # Initialize the simulation object
126     sim = Simulation( Nz, zmax, Nr, rmax, Nm, dt, zmin=zmin,
         n_order=n_order, use_cuda=use_cuda,
128         boundaries={'z':'open', 'r':'reflective'})
         # 'r': 'open' can also be used, but is more computationally
     expensive
130
     # Create the plasma electrons
132     elec = sim.add_new_species( q=-e, m=m_e, n=n_e,
         dens_func=dens_func, p_zmin=p_zmin, p_zmax=p_zmax, p_rmax=
    p_rmax,
134         p_nz=p_nz, p_nr=p_nr, p_nt=p_nt )

136     # Load initial fields
     # Add a laser to the fields of the simulation
138     # Few-cycle laser profile
     profile = FewCycleLaser(a0, w0, tau, z0, zf)
140     add_laser_pulse(sim, profile)

142     if use_restart is False:
         # Track electrons if required (species 0 correspond to the
    electrons)
144         if track_electrons:
             elec.track( sim.comm )
146     else:
         # Load the fields and particles from the latest checkpoint
    file
148         restart_from_checkpoint( sim )

150     # Configure the moving window
     sim.set_moving_window( v=v_window )
```

```
152
    # Add diagnostics
154 sim.diags = [ FieldDiagnostic( diag_period, sim.fld, comm=sim.
    comm ),
                ParticleDiagnostic( diag_period, {"electrons" :
    elec},
156                   select={"uz" : [1., None ]}, comm=sim.comm ) ]
    # Add checkpoints
158 if save_checkpoints:
        set_periodic_checkpoint( sim, checkpoint_period )
160
    # Number of iterations to perform
162 N_step = int(T_interact/sim.dt)

164 ### Run the simulation
    sim.step( N_step )
166 print('lwfa script was executed successfully')
```

Appendix B

Computing resources

B.1 Computing resources

The simulation are done on the computer server at the Division on Atomic Physics at the Faculty of Engineering. For this particular purpose, the simulations were faster on the GPU than the 2×10 CPU. The installed graphics card is a Nvidia GeForce GTX 1050 Ti, originally optimized for gaming purposes, and has total available memory of 4 GB. Since the graphics card is distributed by Nvidia, it supports CUDA (compute unified device architecture), which is a parallel computing platform created by Nvidia. CUDA is specifically designed to communicate with programming languages, such as C, C++, Fortran, etc. [31], and therefore no prior advanced knowledge of graphics card programming is required to operate a code on the GPU. In table B.1, the memory specifications of the graphics card is listed.

Table B.1: *Memory specifications of Nvidia GeForce GTX 1050 Ti.*

Memory speed	7 Gbps
Standard memory configuration	4 GB GDDR5
Memory interface width	128-bit
Memory bandwidth	112 GB/sec